Pliocene-to-Holocene volcano-tectonic activity on Mohéli Island (Comoros archipelago) constrained by new K Ar ages

Anaïs Rusquet, Vincent Famin, X. Quidelleur, Laurent Michon, François Nauret, Martin Danišík, Isabelle Thinon, Sylvie Leroy, Anne Lemoine

Pliocene-to-Holocene volcano-tectonic activity on Mohéli Island (Comoros archipelago) constrained by new K-Ar ages

Anaïs Rusquet[a,b,*], Vincent Famin[a,b], Xavier Quidelleur[c], Laurent Michon[a,b], François Nauret[d], Martin Danišík[e], Isabelle Thinon[f], Sylvie Leroy[g], Anne Lemoine[f]

[a] Université Paris Cité, Institut de Physique du Globe de Paris, 75005 Paris, France

[b] Université de La Réunion, Laboratoire Géosciences Réunion, 97744 Saint Denis, France

[c] Université Paris-Saclay, GEOPS, 91405 Orsay, France

[d] Université Clermont-Auvergne, Laboratoire Magmas et Volcans, 63038 Clermont-Ferrand, France

[e] John de Laeter Centre, Curtin University, 6845 Perth, Australia

[f] BRGM (French Geological Survey), 45060 Orléans, France

[g] Sorbonne Université, CNRS-INSU, Institut des Sciences de la Terre de Paris, 75005 Paris, France

* anais.rusquet@univ-reunion.fr

Keywords

Comoros archipelago, K-Ar dating, Mohéli Island, Holocene volcanism, volcano subsidence, melilitite, Lwandle/Somali plate boundary

Highlights

- New robust K-Ar ages constraints on the volcano-tectonics of Mohéli Island
- Two construction stages at ≥3.8–3 Ma and 2–0.008 Ma, separated by a main subsidence
- Volcano-tectonic shift, from N070°E in Stage 1 to N110°E in Stage 2
- Moderate silica-undersaturation in Stage 1 magmas, high undersaturation in Stage 2
- Holocene volcanism in Mohéli implies that the entire Comoros archipelago is active

Abstract

The volcanism of the Comoros archipelago (from west to east: Grande Comore, Mohéli, Anjouan, and Mayotte islands) has been under renewed scientific scrutiny since the eruption of a new submarine volcanic edifice (Fani Maoré) which begun in May 2018 east of Mayotte. West of Mayotte, Mohéli island has received little attention from the geoscience community, despite its largely uneroded volcanic landscapes suggesting a recent activity that has not been dated. Here we address this gap in knowledge by applying K-Ar geochronology on groundmass and major-trace element analyses to subaerial and submarine rocks, in an attempt to reconstruct the volcano-tectonic and geochemical evolution of Mohéli. Our results show that Mohéli's volcano-tectonic evolution proceeded in two constructional stages, including a primary edification along a N070°E axis from before ca. 3.8 Ma to ca. 3 Ma (Stage 1), and a second construction along a N110°E ridge shaping the present-day island since ca. 2 Ma (Stage 2). The two stages were separated by an increased subsidence (≥0.2 mm/yr) that drowned a large part

of the N070°E primary edifice. The two identified volcano-tectonic stages are reflected also in the geochemical evolution of emitted magmas, which were moderately silica-undersaturated in Stage 1 and moderately to highly silica-undersaturated in Stage 2. Silica undersaturation increases with time up to the olivine melilitite field, together with enrichments in Ca, P, and incompatible trace elements, suggesting the increasing contribution of a metasomatized mantle in melts. The coeval changes of construction orientations and magmas compositions of Mohéli suggest a modification in the tectonics of the Comoros related to magmatism at about 2 Ma. The most recent volcanic morphology investigated is an olivine nephelinite lava flow on the north coast of the island dated at 8 ± 2 ka. This finding of Holocene volcanism on Mohéli implies that the entire Comoros archipelago should be considered as an active zone in any volcanic hazard assessment. The melilite-bearing rocks of Mohéli share geochemical similarities with those of Mayotte and of the Cenozoic volcanic provinces of Madagascar, further pointing to similar melting sources and magmatic processes over the Mozambique channel.

1. Introduction

The Comoros archipelago, located in the northern Mozambique channel (Fig. 1a) has regained attention from the scientific community since 2018 due to the birth of a fast-building submarine volcanic edifice, 50km east of Mayotte, Fani Maoré volcano (Lemoine et al., 2020; Feuillet et al., 2021; Berthod et al., 2021a). Marine geophysical surveys have since revealed that the archipelago is only the emerged portion of a much wider province of volcanic ridges and seamounts extending north and east of the islands (Tzevahirtzian et al., 2021; Thinon et al., 2022). The origin of volcanism in the Comoros archipelago remains enigmatic in many aspects since none of the proposed interpretations can explain all the observations. For instance, the archipelago has been interpreted as an east-to-west propagating hotspot track, related to the moving Somali plate over a mantle plume (Hajash and Armstrong, 1972; Emerick and Duncan, 1982; 1983; Class et al., 2005). This hypothesis is supported mainly by the apparent westward progression of volcanism from Mayotte (eroded and surrounded by a barrier reef) to Grande Comore (hosting the recurrently erupting Karthala volcano), and by the enriched mantle isotopic signature of Grande Comore magmas. However, the NE-directed motion of the Somali plate in an absolute reference frame does not match the E-W alignment of the archipelago, which contradicts the hotspot hypothesis (Fig. 1a). Alternatively, the magmatism of the Comoros archipelago has been interpreted to be controlled by reactivation of deep lithospheric fractures (Nougier et al., 1986). More recently, magmatism has been proposed to delineate the boundary between the Somali and Lwandle plates (Fig. 1a, Stamps et al., 2018; Famin et al., 2020), in connection with the East African Rift System (Michon, 2016; Michon et al., 2022). These tectonic interpretations, however, do not account for the plume-compatible isotopic signature of magmas.

For any discussion about the origin of the Comoros, the chronology of volcanic construction is of central importance. Unfortunately, despite significant effort, radiometric ages reported for the Comoros archipelago are still sparse and unevenly distributed. The majority of geochronological data come from Mayotte and include 33 K-Ar whole-rock ages (Hajash and Armstrong, 1972; Emerick and Duncan, 1982; 1983; Nougier et al., 1986) and 24 groundmass $^{40}Ar/^{39}Ar$ (Pelleter et al., 2014). The island of Anjouan has been the subject of recent geochronological investigations by Quidelleur et al. (2022), resulting in an updated database of 13 new K-Ar ages on groundmass, 5 K-Ar whole-rock ages, and one ^{14}C age. This most recent study revealed the occurrence of Holocene volcanism in Anjouan, but also demonstrated that

whole-rock K-Ar dating of Comorian magmatic rocks is challenging due to the presence of xenoliths, which may affect the accuracy of results. In comparison, only 10 ages are available for Mohéli and 2 for Grande Comore (Hajash and Armstrong, 1972; Emerick and Duncan, 1982; 1983; Nougier et al., 1986), all obtained by K-Ar whole-rock analyses made prior to the development of the K-Ar Cassignol-Gillot technique on groundmass (Gillot and Cornette, 1986; Gillot et al., 2006). Regarding the hypothesis of a geographic migration of volcanism in the Comoros, it is therefore important to ascertain the accuracy of existing ages and to build a robust and more complete geochronological database on these two islands.

In this study, we focus on Mohéli because this island displays both eroded reliefs and developed carbonate platforms like in Mayotte, but also well-preserved volcanic morphologies similar to those of Anjouan (Fig. 1b). These contrasting morphologies indicate a protracted volcanic activity on Mohéli, spanning from the early construction of the Comoros archipelago up to very recent times. The objective of this study is to develop a more robust geochronological framework for the volcano-tectonic evolution of Mohéli, by providing new radiometric data for the different morphologies. For that purpose, we adopted a multi-disciplinary approach that involved geomorphological fieldwork, K-Ar dating of groundmass by the Cassignol-Gillot technique, and major-trace element analyses of whole rocks. In addition, we also took advantage of the offshore bathymetric surveys, reflection seismic profiles and dredges performed during the oceanographic cruise SISMAORE onboard R/V Pourquoi Pas? (Thinon et al., 2021) to investigate the submarine slopes of the Mohéli edifice. The joint use of geomorphological, geochronological, and geochemical data on submarine and subaerial reliefs allows us to reconstruct the volcano-tectonic history of Mohéli, with implications for the geodynamics and volcanic hazards of the Comoros archipelago.

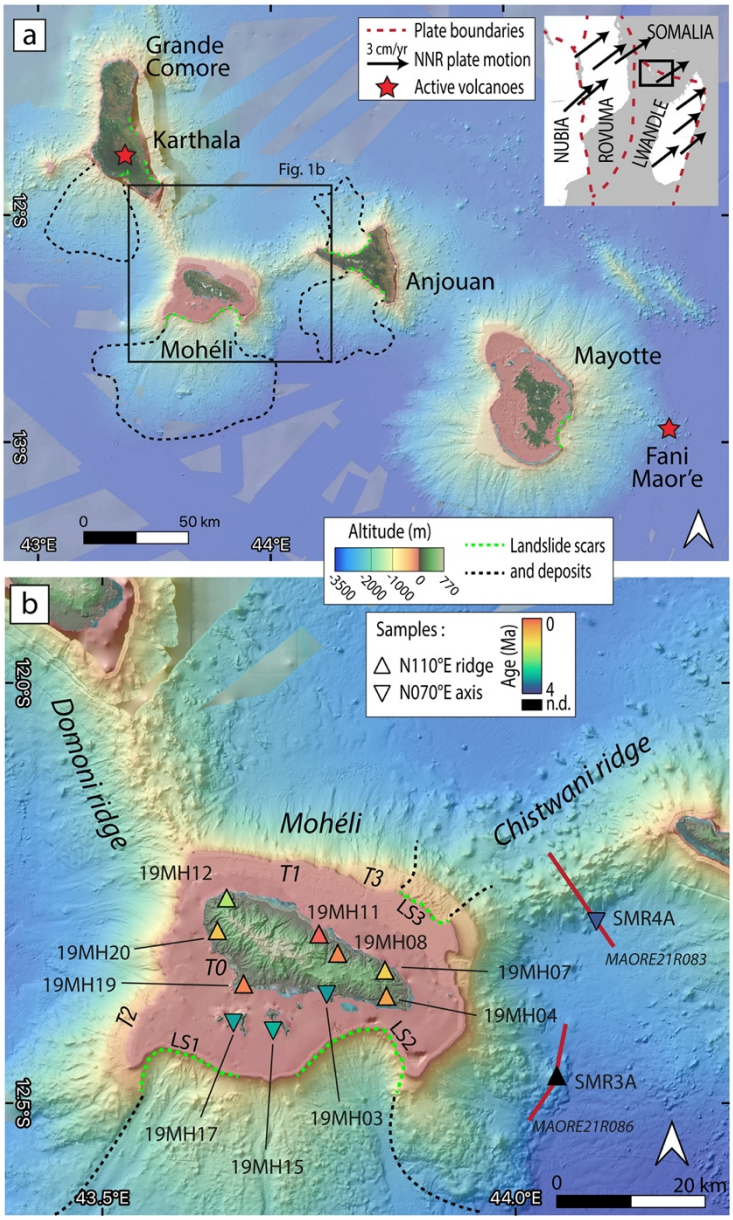

Figure 1: a- Map of the Comoros archipelago, bathymetric compilation (from Tzevahirtzian et al., 2021 and references therein; MAYOBS campaigns Rinnert et al., 2019; Ifremer Geo-ocean, 2022; Thinon et al., 2022; Berthod et al., 2021b, and GEBCO data), GNSS plate motions in a no-net rotation (NNR) framework (King et al., 2019). b- Topographic and bathymetric map of Mohéli and the Chistwani ridge showing the location of analyzed samples. Also shown are fringing reef (T0), carbonate shelves (T1 to T3), landslide scars (LS1 to LS3), and landslide deposits recognized by Tzevahirtzian et al. (2021). The color and orientation of triangles correspond to the age of samples and their attribution to volcanic lineaments, respectively, as shown in the legend. Red lines correspond to the location of seismic reflection profiles MAOR21R086 and MAOR21R083.

2. Geological setting

The Comoros archipelago is located on the northern part of the Mozambique Channel, to the east of Mozambique and northwest of Madagascar (Fig. 1). The Comoros archipelago is considered to be built on an oceanic lithosphere (e.g. Phethean et al., 2016; Rolandone et al., 2022; Masquelet et al., 2022), although there is debate about the possible existence of a continental remnant of Madagascar's drift underneath Mayotte (Dofal et al., 2022). According

to trace element compositions and Sr-Nd-Pb isotopic ratios, the magmas of Mohéli, Anjouan, and Mayotte may be explained by mixing of a high $\mu = {}^{238}U/{}^{204}Pb$ (HIMU) component and a depleted MORB-mantle (DMM) component at variable degrees of partial melting (Späth et al., 1996; Pelleter et al., 2014; Bachèlery and Hémond, 2016). Grande Comore is the only island showing isotopic evidence of a plume contribution in magmas added to the HIMU and DMM components (Class et al., 2005 and references therein, see Bachèlery and Hémond, 2016 for a review). None of the Comorian lavas displays any evidence of continental crust contamination (e.g. Bachèlery and Hémond, 2016). The HIMU signature is sought to be introduced in the Comorian mantle reservoir through delamination or thermal erosion of a continental lithosphere during Gondwana break-up (Späth et al., 1996; Class et al., 2005; Pelleter et al., 2014; Bachèlery and Hémond, 2016). Incompatible element relative enrichments of all the magmatic products throughout the Comoros indicate that metasomatism of the HIMU-DMM mantle is a common feature of all the parental magmas (Späth et al., 1996; Deniel, 1998), an inference confirmed by CO_2-metasomatized mantle xenoliths found in Grande Comore (Coltorti et al., 1999). CO_2 metasomatism is also supported by the occurrence of P-rich olivine melilitites (i.e., alkaline and ultracalcic mafic igneous rocks rich in melilite, a calcic sorosilicate, and devoid of feldspar) on the northwest side of Mayotte (Pelleter et al., 2014). Building on partial melting experiments that position the origin of melilititic primary melts in the domain of garnet stability, in the presence of CO_2, at pressures ranging from 3 to 4 GPa (Dasgupta et al., 2007; Gudfinnsson and Presnall, 2005; Hirose, 1997), Pelleter et al. (2014) have interpreted melilite-bearing magmas as coming from very low partial melting of apatite-dolomite-rich zones in the CO_2-metasomatized lithospheric mantle. A similar conclusion was reached for the origin of Cenozoic melilitites from northern, central, and eastern Madagascar (Melluso et al., 2011; Cucciniello et al., 2016; Mazzeo et al., 2021). Though undated, olivine melilitites are thought to be related to rifting on Mayotte during the postshield stage (<4 Ma, Pelleter et al., 2014).

Mohéli is considered to be one of the oldest islands in the archipelago, along with Mayotte, based on its eroded reliefs and its well-developed insular shelves (Fig. 1; Tzevahirtzian et al., 2021). The history of Mohéli has been subdivided into two volcanic stages and three series (Pavlovsky and De Saint Ours, 1953; De Saint Ours, 1960; Esson et al., 1970; Strong, 1972a). De Saint Ours (1960) noticed the radiating shape of elongated islets and extended promontories on the south coast. He suggested that these morphologies represent valleys eroded into the flanks of an early sub-circular volcano, later filled with lava flows. The products of this early volcano, mostly basanitic, have been classified as a basal or lower series. In a later stage, repeated eruptions along WNW fissures shaped the present-day N110°E elongation of the island, with rugged topographies attributed to an intermediate series of hawaiites, basanites, and ankaramites, and more subdued reliefs of an upper series of olivine nephelinites and basalts. Based on K-Ar whole-rock dating, Nougier et al. (1986) estimated the lower, intermediate and upper series to be >5 Ma, 3.8–3.2 Ma, and 2–0.5 Ma old, respectively. The composition and differentiation trends of Mohéli's magmatic products are thus relatively similar to those of Mayotte (Bachèlery and Hémond, 2016), even though highly-silica undersaturated rocks such as melilitites have not been described yet.

Bathymetry map shows that the submarine slopes of Mohéli are prolongated by two ridges (Fig. 1), a N160°E "Domoni ridge" on the northwest connecting Mohéli to Grande Comore, and a N055°E "Chistwani ridge" on the northeast connecting Mohéli to Anjouan (Thinon et al., 2022; Tzevahirtzian et al., 2021). Two submarine terraces are described at 400 to 600 m depth on the southwestern and northeastern slopes of Mohéli's edifice (T2 and T3 in Fig. 1b; Tzevahirtzian et al., 2021). These terraces indicate that a strong subsidence affected Mohéli prior to the construction of the main shelf (T1). Mohéli is also surrounded by a fringing reef (T0) found on many islands of the Indian Ocean and known to be constructed by the last sea level rise since

8-9 ka (Camoin et al., 2004). Two landslide scars (LS1 and LS2 in Fig. 1b) also affect the southern flank of the submarine edifice, cutting both the subsided terraces and the modern shelf. A third, smaller landslide scar (LS3) also cuts T1 north of Mohéli, with debris avalanche deposits on T3.

3. Methods

3.1 Sampling

Samples of volcanic rocks for geochronological and geochemical investigations were first collected onshore on Mohéli Island during a field trip in 2019 (samples labelled 19MHXX, Fig. S1). Great care was taken to select only massive rock samples with the best possible freshness and the lowest vesicularity on visual inspection, as these two selection criteria are of paramount importance for successful K-Ar dating. Three samples belong to the islets and eroded remnants of the flanks of the early volcano on the southern coast of Mohéli (Fig. 1b). Three other samples were collected on eroded flanks, often covered with lateritic soils, forming the N110°E-elongated shape of the island. Four other samples were taken from uneroded volcanic features throughout the island, such as Strombolian volcanic cones and lava flows barely covered by soils.

Two offshore sites were dredged east of Mohéli during the SISMAORE oceanographic cruise (Thinon et al., 2021). The first dredge site is located on a ~500 m-tall volcanic cone at the base of the Mohéli edifice in the eastward prolongation of its N110°E axis (SMR3, Fig. 1b). The 48-channel seismic reflection profiles show an acoustic basement covered sometimes by a thin layered seismic unit, which is interpreted as shallow sediment or volcano-sediment deposits. This acoustic basement across the volcanic cone east of Mohéli (Fig. 2a) and across the Chistwani ridge (Fig. 2b), characterized by unreflective seismic facies (no coherent reflectors) and at its top by an irregular surface with high amplitude, is assumed to be magmatic in nature (Thinon et al., 2022; Masquelet et al., 2022). In addition to weakly-consolidated carbonate sediment, dredge SMR3 collected polygenic volcanic products including rounded pebbles of basalt covered by 1 mm-thick iron-manganese oxide concretions, blunted-edged cobbles of altered ankaramite volcanic breccia, and fresh, angular fragments of aphyric basalt pillow lavas (Thinon et al., 2021). As these latter elements are the freshest of the dredge and show no trace of transport, they were selected for further analyses (sample SMR3A, Fig. S1). The other dredge site is a ~300 m-high cliff on the southern flank of the Chistwani ridge (SMR4, Fig. 1b), cliff shown on the seismic profile (Fig. 2b). Dredge SMR4 recovered indurated and unconsolidated carbonate sediment and polygenic volcanic products, but only as angular elements indicating an absence of significant sedimentary transport (Thinon et al., 2021). The recovered volcanic products include elements of palagonitized olivine basalt volcanic breccia, and fragments of unaltered, olivine basalt pillow lavas selected for geochronology and chemical analyses (sample SMR4A; Fig. S1).

Subaerial and submarine samples underwent a second selection for K-Ar dating at the GEOPS laboratory (Orsay, France) based on thin section observation (Fig. S2). Sample SMR3A did not pass this second selection as it showed evidence of minor alteration. Consequently, SMR4A was the only remaining submarine sample deemed suitable for K-Ar dating.

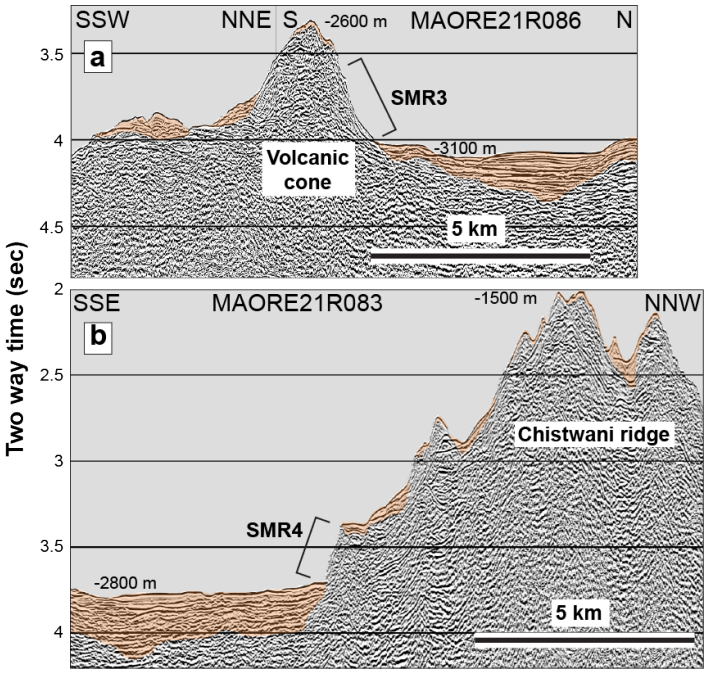

Figure 2: Sections of time-migrated 48-channel seismic reflection profiles MAOR21R086 across the volcanic cone east of Mohéli dredged by SMR3 (a) and MAORE21R083 across the Chistwani ridge dredged by SMR4 (b), represented at the same scale with vertical exaggeration ~5.4 using velocity of 1500 m/s (see Fig. 1b for location). Orange layers represent the shallow sedimentary deposits on the acoustic basement interpreted as volcanic. The seismic reflection profiles and dredges have been acquired during the SISMAORE campaign (Thinon et al., 2021). Note, at the toe of the volcanic cone or the cliff, the acoustic basement is onlapped by a layered seismic unit (thick of ~0.1 sec in two-way travel time). On the abrupt slopes, the acoustic basement outcrops.

3.2 K-Ar dating

Thin sections of the 11 samples (10 subaerial and 1 submarine) selected for K-Ar dating were inspected to determine which fraction size would be the most suitable for analysis based on the size and abundance of phenocrystals (Fig. S2). The K-Ar technique applied to carefully separated groundmass has the main advantage of avoiding the drawbacks of sample irradiation and its recoil effect and interfering production of ^{36}Ar, which affects the precision of $^{40}Ar/^{39}Ar$ dating applied to young (<1 Ma), low-K and high-Ca-rich rocks such as basalts (Gillot et al., 2006). For this reason, the K-Ar technique on groundmass is the most powerful technique for dating volcanic rocks in the Holocene realm in the absence of material suitable for other techniques such as charcoal for ^{14}C, or zircon for (U-Th)/He. K-Ar on groundmass has been successfully applied to many Holocene low-K volcanic rocks ($K \leq 2$ wt.%), including Chimborazo volcano in Ecuador (4 ± 2 ka; Bablon et al., 2019), Merapi volcano in Indonesia (4.8 ± 1.5 ka; Gertisser et al., 2012), Guadeloupe Island in the Lesser Antilles (6 ± 2 ka; Samper et al., 2009), Tromen volcano in Argentina (7 ± 2 ka; Pallares et al., 2019), and Etna volcano in Italy (10 ± 3 ka; Blard et al., 2005). Recently, Quidelleur et al. (2022) have documented Holocene volcanism in Anjouan (Comoros) by dating a lava flow by K-Ar at 11 ± 1 ka, which, together with a tephra dated by ^{14}C at 9.2 ± 0.3 ka, demonstrate that volcanism is sub-active in this island. Consequently, we have applied here the K-Ar technique to carefully selected groundmass separated from submarine and subaerial samples. In both cases, the outer parts of the samples in contact with water or air were removed, to prevent the incorporation of K from seawater, and of excess radiogenic ^{40}Ar from the outermost few cm of rapidly cooled rocks (e.g., Duncan and Hogan, 1994).

Samples were manually crushed and sieved, and ultrasonically cleaned in a 10% HNO_3 solution. Selected fractions were isolated within a narrow density interval by heavy liquid separation using diiodomethane, to remove dense xenocrysts and the lightest phases in the eventuality of undetected alteration. Indeed, the incorporation of xenocrysts or altered phases may yield calculated K-Ar ages older than the "true" ages. Potassium and Ar measurements were acquired following the unspiked Cassignol-Gillot method (Cassignol and Gillot, 1982; Gillot and Cornette, 1986; Gillot et al., 2006), with duplicated measurements. The K content for each sample was measured via flame-absorption spectrometry with BCR-2 (Raczek et al., 2001; K = 1.481 %) and MDO-G (Gillot et al., 1992; K = 3.51 %) as reference standards. Argon, along with other gases, was extracted after complete melting of the sample at high temperature (above 1400°C). Then, a three-step procedure was followed to remove all gases but noble gases (i.e., mainly Ar). First, gas clean-up was performed with a large amount (15 g) of pure Ti foam heated at 800°C for one hour, then cooled to room temperature for about 20 min. Two successive clean-up steps of 2 min long each were then performed using Al-Zr AP10GP SAES getters to further purify gases prior to analysis. Argon 36 and 40 isotopes were measured using a multi-collector 180° sector mass spectrometer by comparing the samples and atmospheric aliquots (for details see Germa et al., 2010). The ^{40}Ar signal was calibrated by an air pipette compared to the HD-B1 standard (Fuhrmann et al., 1987; Hess and Lippolt, 1994) using the age of 24.18 Ma (Schwarz and Trieloff, 2007). The ^{40}K decay constants and K isotopic ratio of Steiger and Jäger (1977) were used for calculation. Age uncertainties reported here are at the 1σ level, unless otherwise stated.

For the submarine sample SMR4A, we applied the approach of Henri et al. (2022) to get rid of possible seawater Ar contamination. Prior to Ar measurements, the submarine sample was pre-degassed during 30 min at low temperature (about 200°C) to remove superficial Ar contamination. This protocol was set after multiple trials to make sure no radiogenic Ar was lost through the process (see Henri et al., 2022 for details).

3.3 Major and trace element geochemistry

The 12 samples (10 subaerial and 2 submarine, including SMR3A rejected for K-Ar dating) were analyzed for major and trace elements, to classify the rocks according to international charts, as well as to compare their chemistry with the existing literature. Whole-rock major and trace elements measurements were conducted at the University of Bretagne Occidentale (Brest, France) via ICP-AES (Thermo Electron IRIS Advantage) and ICP-MS (Thermo Elemental x7). Prior to analysis, samples were fused with $LiBO_2$ in Pt-Au crucibles before being dissolved with HNO_3. International standards used for calibration (BCR-2 and BHVO-2) underwent the same process as samples (Carignan et al., 2001). Relative 2σ uncertainties are lower than 2% for major elements and lower than 5% for trace elements. Geochemical major and trace elements data from the surrounding islands of Grande Comore (Flower, 1971; Strong, 1972b; Späth et al., 1996; Class and Goldstein, 1997; Claude-Ivanaj et al., 1998; Deniel, 1998; Class et al., 1998, 2005), Mohéli (Strong, 1972a; Nougier et al., 1986; Späth et al., 1996), Anjouan (Thompson and Flower, 1971; Flower, 1971, 1973; Nougier et al., 1986; Quidelleur et al., 2022) and Mayotte (Nougier et al., 1986; Späth et al., 1996; Pelleter et al., 2014), were extracted from the GEOROC database for comparison purposes with our new samples.

4. Results

4.1 K-Ar dating results

New K-Ar ages on 11 samples range from 3.738 ± 0.054 Ma to 8 ± 2 ka (Table 1). Potassium content of the groundmass ranges between 0.922% and 2.037%, and radiogenic ^{40}Ar between 0.3% and 61.5%. For subaerial Mohéli samples, three ages fall in the 3.3–3.1 Ma range (19MH03, 19MH15, and 19MH17), one is at 1.845 ± 0.026 Ma (19MH12), and seven are younger than 1.050 Ma (19MH04, 19MH07, 19MH08, 19MH11, 19MH19, and 19MH20). One sample (19MH11) revealed a Holocene age of 8 ± 2 ka. Submarine sample SMR4A from the Chistwani ridge gave an age of 3.738 ± 0.054 Ma, which is slightly older than the oldest ages measured on subaerial Mohéli samples.

4.2 Major and trace element chemistry

Major and trace element data are reported in Table 2 and displayed in Figures 3 and 4 together with literature data. In a total alkali versus silica (TAS) diagram with the sum of oxides normalized to 100 wt.% (Fig. 3a), all our analyses are in the field of alkali series, consistent with published analyses. Subaerial samples from Mohéli fall in the fields of basalts (19MH03, 19MH07, 19MH15, and 19MH17), basanites (19MH04 and 19MH20), and in the undersaturated field of foidites (19MH08, 19MH11, 19MH12, and 19MH19). The two submarine samples are very close in major-element composition to subaerial data from the literature and from the present study. Sample SMR3A, from the volcanic cone at the base of Mohéli, is at the junction of the foidite and tephri-basanite fields, close to published analyses from subaerial Mohéli. Sample SMR4A, from the Chistwani ridge, is in the basanite/basalt field, and within the field of subaerial data from Mohéli as well as Anjouan. Except SMR3A, all the samples from Mohéli have losses on ignition (LOIs) of -0.29 to 2.87 wt.%, in the lower range of fresh basanites, nephelinites, and melilitites (e.g. Jung et al., 2019). In particular, 19MH11, the sample which yields the youngest K-Ar age of 8 ± 2 ka, is also the one with the most negative LOI of -0.29 wt.%, typical of freshly emitted lavas from Karthala (e.g. Späth et al., 1996; Class et al., 2005). Sample SMR3A has a LOI of 4.94 wt.%, about 1.5 wt.% above unaltered foidite (e.g. Mertz et al., 2015).

Mafic rocks (MgO > 5%) are presented in the basanite-nephelinite-melilitite classification schemes of Woolley et al. (1996) to highlight their undersaturated composition (Fig. 3b). In a $CaO + Na_2O + K_2O$ vs $SiO_2 + Al_2O_3$ diagram, some samples fall in the field of nephelinites (19MH04, 19MH08, and 19MH20) and others in the field of melilitites (19MH11, 19MH12, and 19MH19). All are subaerial and from the mainland of Mohéli. According to Woolley et al. (1996), CIPW normative larnite ($_N$larnite: Ca_2SiO_4, the calcic pole of melilite) may be used to further classify olivine nephelinites (<10% $_N$larnite) from olivine melilitites (≥10% $_N$larnite). Among the samples that can be represented in this classification, one (19MH19) is an olivine melilitite at 12% $_N$larnite, whereas the others (19MH08, 19MH11, and 19MH12) are in the field of olivine nephelinites.

In spider diagrams normalized to primitive mantle (Fig. 4), our new data from Mohéli and the Chistwani ridge plot within the range of those published for the less silica-rich rocks of this island (i.e., for SiO_2 < 50 wt.% after oxide sum normalization to 100%), except for U, Ta, and Pb for which there is no literature data. Nevertheless, our data may be subdivided in two groups. The first group of five samples (SMR4A, 19MH03, 19MH07, 19MH15, and 19MH17) shows a moderate enrichment in the most incompatible elements relative to primitive mantle, whereas a second group of seven samples (SMR3, 19MH04, 19MH08, 19MH11, 19MH12, 19MH19, and 19MH20) display steeper slopes in spider diagrams and hence stronger enrichments.

Plotted as a function of time, major element concentrations such as $CaO + Na_2O + K_2O$, or concentration ratios of highly to moderately incompatible trace elements such as Ba/Ti or La/Yb, show an evolution of Mohéli's erupted products toward increased proportions of incompatible elements (Fig. 5a-c). Other ratios such as Nb/U, Ce/Pb, or Ta/Th do not show any

obvious correlation with time (Fig. 5d-f). Nb/U and Ce/Pb generally fall between the ranges of normal MORB/OIB (Nb/U ~ 47 ± 10, Ce/Pb ~25 ± 5, Ta/Th >0.6) and HIMU (Ce/Pb ~28 – 48, 0.4 < Ta/Th <0.6, Hofmann, 1997; Willbold and Stracke, 2006; Farmer et al., 2020).

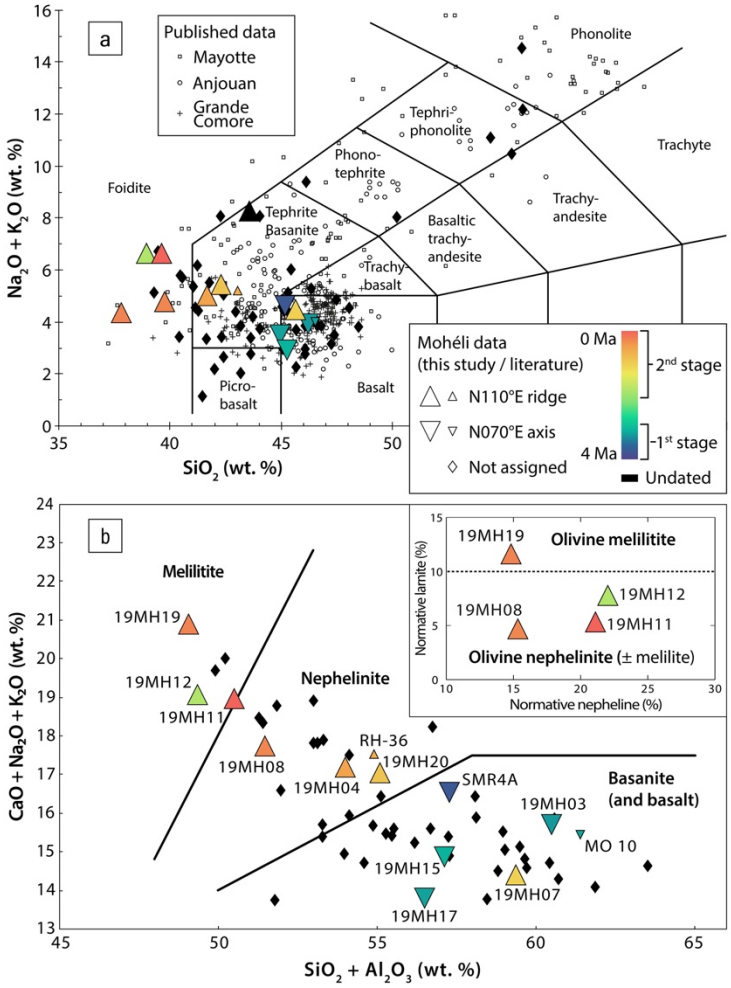

Figure 3: a- Major element compositions of Mohéli and Chistwani ridge samples represented in a total alkali versus silica (TAS) diagram (Le Bas et al., 1986) compared with volcanic rocks from the Comoros islands (GEOROC database and Quidelleur et al., 2022). b- Melilitites classification diagrams for mafic samples (MgO > 5 wt.%, after Le Bas, 1989 and Woolley et al., 1996). Also added are the two literature samples with validated K-Ar whole-rock ages and available major ± trace element data (MO10 from Nougier et al., 1986, and RH-36 from Emerick and Duncan, 1982, 1983 with major and trace element data from Späth et al., 1996). The color chart of symbols refers to the K-Ar age of samples.

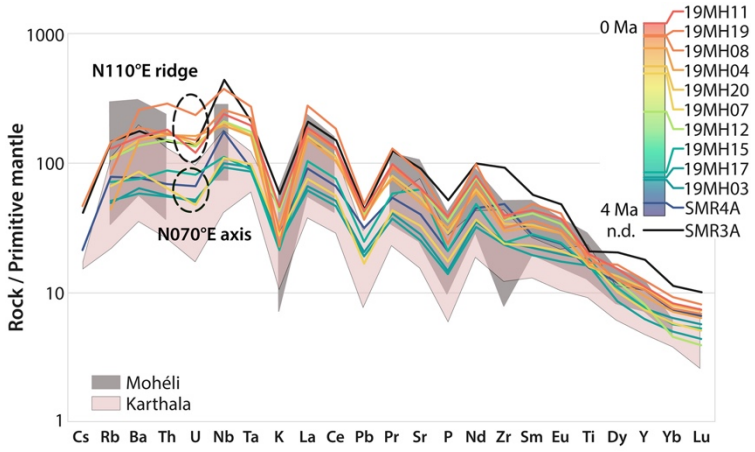

Figure 4: Spider diagram of trace element concentrations in the studied samples, normalized to primitive mantle (using the values of Lyubetskaya and Korenaga, 2007). The grey and pink fields correspond to published data for Mohéli Island and Karthala volcano, respectively (GEOROC database). The color chart refers to the K-Ar groundmass age of each sample, except for SMR3A (not dated, n.d.). The N070°E axis and N110°E ridge correspond to the two volcano-tectonic stages of Mohéli's edification.

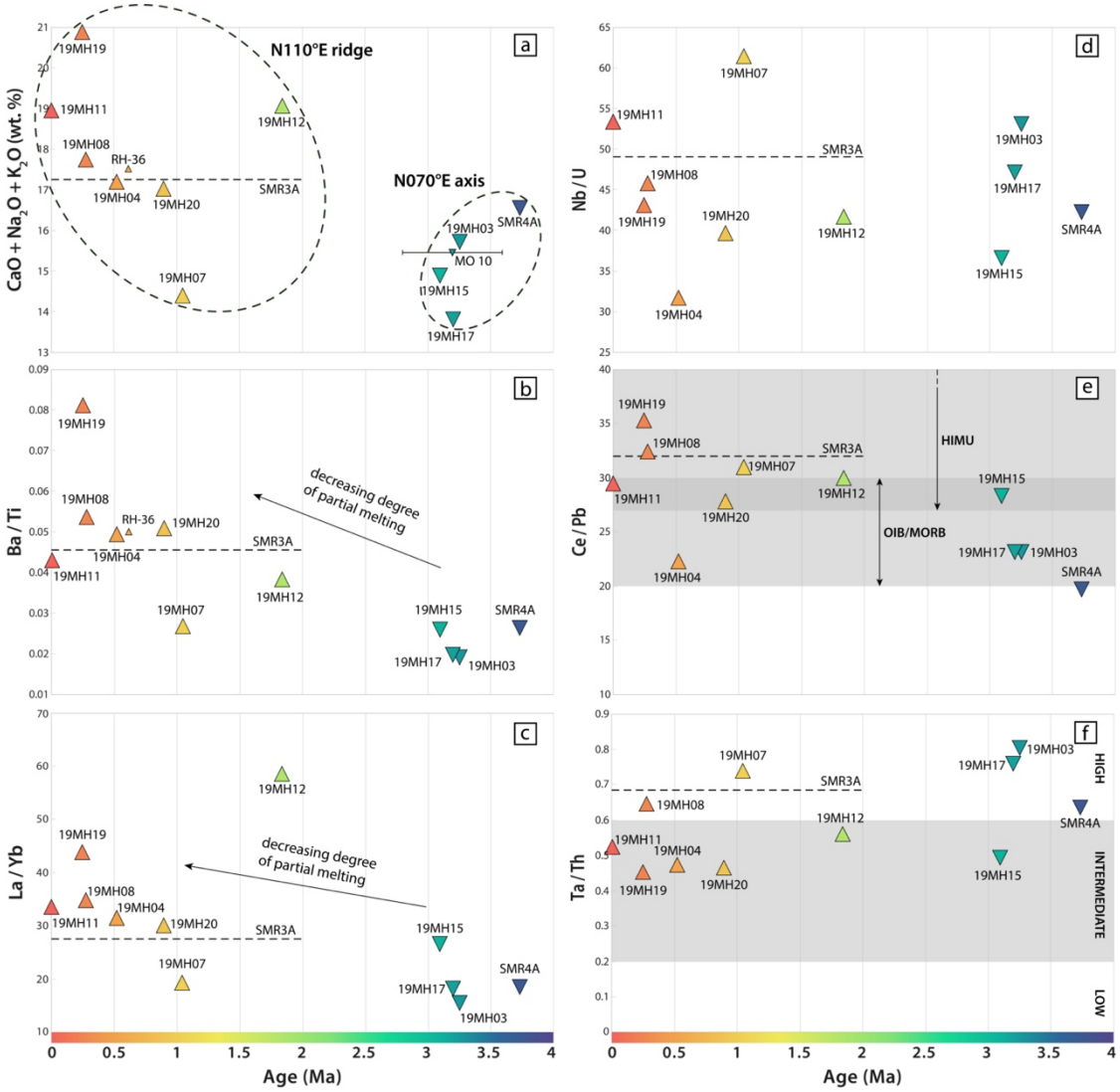

Figure 5: $CaO+Na_2O+K_2O$ concentration (a), Ba/Ti ratio (b), La/Yb ratio (c), Nb/U (d), Ce/Pb (e), and Ta/Th (f) of dated samples as a function of time. Color chart is the same as in Figs 1 – 4. Also included are literature data for samples whose age and major or trace elements are available (MO10 from Nougier et al., 1986; RH-36 from Emerick and Duncan, 1982, 1983; Späth et al., 1996). Error bars are smaller than symbol size, except for MO10. Also represented are values for sample SMR3A (grey dashed line), undated but interpreted as belonging to the second stage N110°E ridge according to its location and chemistry. The Ce/Pb compositional fields for OIB/MORB and HIMU are from Hofmann (1997) and Willbold and Stracke (2006), and high/intermediate/low Ta/Th fields are from Farmer et al. (2020).

5. Discussion

5.1 Comparison with published ages

As already discussed in Quidelleur et al. (2022), whole-rock K-Ar dating may be prone to inaccuracy due to the presence of excess Ar in xenocrysts, or to K loss and contamination by atmospheric Ar in alteration phases, leading to calculated ages older than the "true" ages. This is especially true for volcanic rocks of the Comoros islands, including Mohéli, because they

contain large quantities of peridotite and/or quartzite xenoliths (Lacroix, 1922; De Saint Ours, 1960; Flower and Strong, 1969; Montaggioni and Nougier, 1981). As a matter of fact, several whole-rock K-Ar ages from Anjouan (Hajash and Armstrong, 1972; Emerick and Duncan, 1982; 1983; Nougier et al., 1986) have been found in disagreement with paleomagnetic polarities (Hajash and Armstrong, 1972) and with K-Ar ages on groundmass using the Cassignol-Gillot technique, the two latter being concordant with each other (Quidelleur et al., 2022). We therefore first compare our new Cassignol-Gillot K-Ar data on groundmass with published ages on Mohéli.

Ten whole-rock K-Ar ages have been reported from Mohéli (Emerick and Duncan, 1982, 1983; Nougier et al., 1986). Our age of 3.258 ± 0.046 Ma on aphyric basalt sample 19MH03 from the southern shore of Mohéli is in excellent agreement with the age of 3.2 ± 0.4 Ma reported by Nougier et al. (1986) for an aphyric basalt (their sample MO 10) from the same locality (Fig. 6). Our sample 19MH07, a lava flow of aphyric basalt from the northeast coast of Mohéli dated at 1.050 ± 0.015 Ma, is located near the samples RH-21 and RH-22 of Emerick and Duncan (1982, 1983) dated at 1.53 ± 0.12 Ma and 1.89 ± 0.02 Ma, respectively (Fig. 6). Our K-Ar age on groundmass is thus 0.5 to 0.9 Ma, respectively, younger than the two whole-rock ages in this area, even though all the samples are located on the same geomorphological structure and have similar compositions. A similar discrepancy is observed on the north coast of Mohéli, between our sample 19MH08 (0.282 ± 0.010 Ma), of which age is younger and more precise than the samples MO 04 and MO 05 of Nougier et al. (1986) dated at 0.56 ± 0.2 Ma and 0.48 ± 0.15 Ma, respectively, collected at the same location. Finally, our sample 19MH12 (1.845 ± 0.026 Ma) on the northwest coast of Mohéli is also younger than the age of 2.75 ± 0.13 Ma reported by Emerick and Duncan (1982, 1983) for the same morphological unit (their sample RH-32). These three examples provide typical cases where thorough groundmass selection yielded younger, more precise, and likely more accurate ages than whole-rock analyses due to their possible contamination by xenocrysts and/or the incorporation of weathered phases.

We note the existence of two ages available in the same area of the northern flank of Mohéli, in a zone we did not investigate (Fig. 6a): a basanite dated at 5.0 ± 0.4 Ma (sample MO 12 in Nougier et al., 1986) and a boulder of unknown composition dated at 1.14 ± 0.08 Ma (RH-42 in Emerick and Duncan, 1982, 1983). These ages differ by nearly 4 Myrs despite being collected on the same geomorphological feature. Furthermore, the 5.0 ± 0.4 Ma age is much older than our groundmass ages of 1.845 ± 0.026 Ma (sample 19MH12) and 0.900 ± 0.015 Ma (19MH20) obtained on the same western massif from geomorphological features with a similar erosional surface (Fig. 6a). Finally, our submarine sample from the Chistwani ridge, likely related to the early volcanism of Mohéli (see below), is only 3.738 ± 0.054 Ma old (SMR4A). Collectively, this evidence suggests that the age of 5.0 ± 0.4 Ma is inaccurate.

The cross-comparison of whole-rock K-Ar ages among themselves, with new groundmass K-Ar ages, and with geomorphological criteria of relative chronology demonstrates that whole-rock K-Ar ages are often “too old” compared to other techniques, and should be regarded only with great caution, a conclusion already reached for samples from Anjouan (Quidelleur et al., 2022) and from other locations (e.g., Quidelleur et al., 1999; Samper et al., 2007). Based on the discussion above, six out of ten whole-rock ages (i.e., RH-21, RH-22, RH-32, MO 04, MO 05, and MO 12) are excluded from the geochronological database of Mohéli for interpretation purposes. Three ages (RH-42: 1.14 ± 0.08 Ma; RH-33: 0.71 ± 0.12 Ma; RH-36: 0.62 ± 0.02 Ma; Emerick and Duncan, 1982; 1983) are not categorically invalidated, and only one age (MO10: 3.2 ± 0.4 Ma; Nougier et al., 1986) is confirmed by our new data.

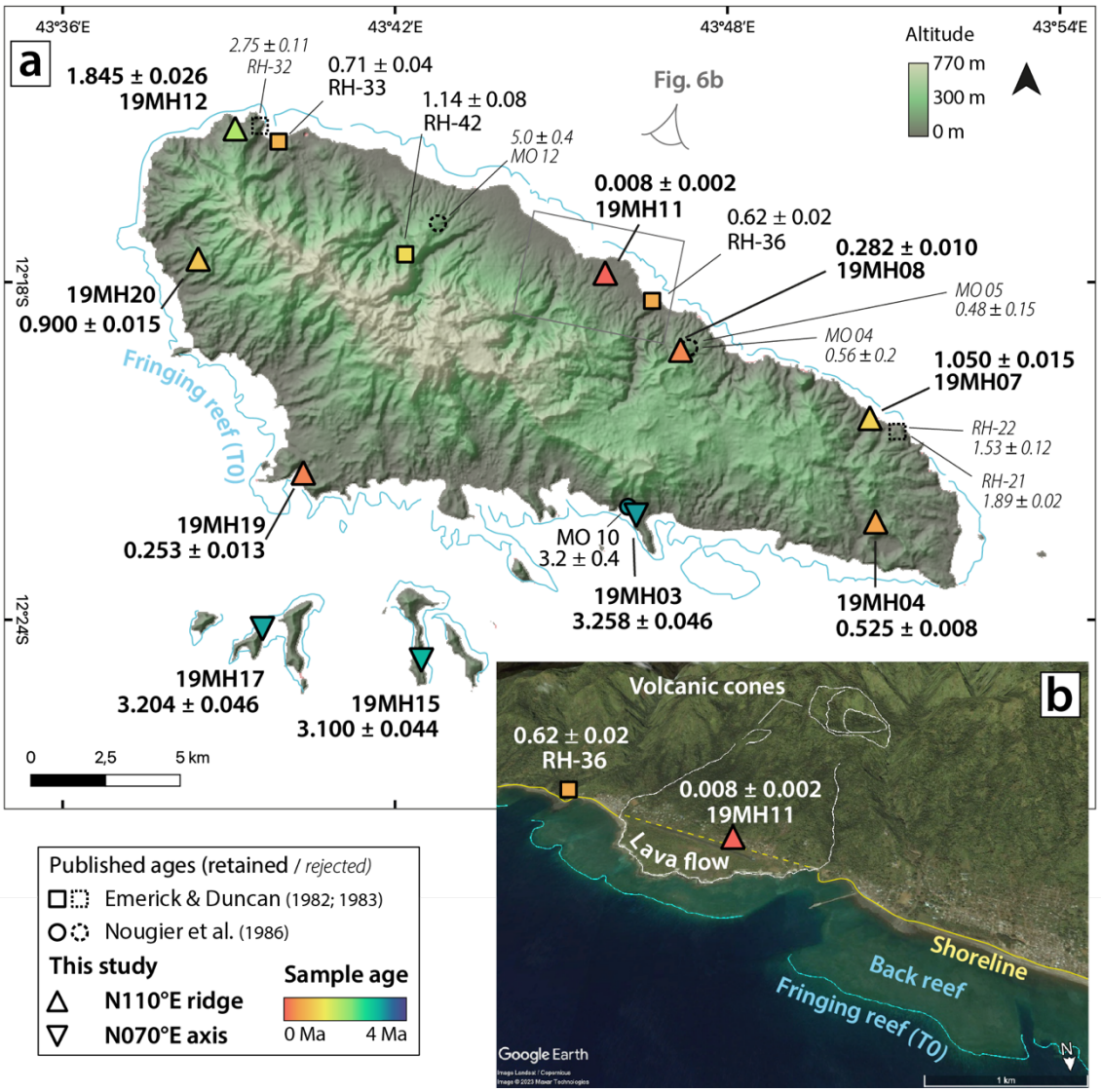

Figure 6: a- Topographic map of Mohéli showing new groundmass K-Ar ages, together with retained and rejected published whole-rock K-Ar ages. b- Google Earth view of the Fomboni airport lava flow (at ×2 vertical exaggeration). Ages and 1σ uncertainties are quoted in Ma.

5.2 Volcanic history of Mohéli and the Chistwani ridge

Based on the 11 new and 4 revised K-Ar ages from subaerial and submarine samples from Mohéli and the Chistwani ridge, we propose that at least two construction stages shaped the submarine and subaerial slopes of Mohéli (Fig. 7). The first stage (Stage 1), starting before 3.8 and lasting to ca. 3 Ma, corresponds to the construction of volcano-tectonic structures along a N070°E axis. The Chistwani ridge was edified in this stage as inferred from age of 3.738 ± 0.054 Ma (sample SMR4A). The drowned carbonate platform T3 covering the SW tip of the ridge (Fig. 1b) indicates that the Chistwani ridge predates the construction of Mohéli's edifice. Stage 1 also includes the edification of the early volcano forming the southern flank of Mohéli, probably concomitant with the activity of the Chistwani ridge. As noticed by Saint Ours (1960), radial islets and peninsulas of the south coast of Mohéli are eroded remnants of the early volcano. These morphological features are inverted topography, in which valleys were infilled by lavas dated at 3.3–3.1 Ma (Fig. 6). Therefore, the early volcano of Mohéli must have been emerged and eroded before 3.3 Ma (Fig. 7). At that time, this early volcano was roughly of

elliptical shape according to the SW and NE tips of the submarine slopes supporting the T2 and T3 drowned platforms, with an eruptive center aligned in the N070°E prolongation of the Chistwani ridge (Fig. 1b). Stage 1 ended up after the filling of erosional valleys ca. 3 Ma ago, and was followed by a period of volcanic quiescence and subsidence (see below).

Stage 2 of the volcano-tectonic construction, postdating the N070°E morphology, corresponds to the N110°E elongated ridge shaping the present-day subaerial island (Figs 1b, 6a). The oldest age within this second stage is at 1.845 ± 0.026 Ma, which suggests a volcanic renewal starting at ca. 2 Ma (Fig. 6). However, a majority of the ages belonging to this stage are in the range 1.14–0.25 Ma, which we consider as the main phase of reconstruction of subaerial Mohéli (Fig. 7). Unfortunately, alteration in sample SMR3A prevented any K-Ar dating to be attempted. However, given the location of the SMR3 volcanic cone in the eastern prolongation of Mohéli's N110°E ridge, we attribute the edification of this seamount to the volcano-tectonic Stage 2. There may have been some periods of low volcanic activity during Stage 2 where ages are currently lacking, for instance in the intervals 1.8–1.1 Ma, 0.52–0.28 Ma, and 0.25–0.008 Ma (Fig. 7), hence additional fieldwork and geochronological data are required to confirm that these hiatuses are true volcanic lulls. Importantly, there are many uneroded volcanic morphologies on the northern and eastern sides of Mohéli, indicating that Stage 2 was still active until very recent times. One of these features is a fresh lava flow on the north coast, on which the airport was built, which we dated at 8 ± 2 ka (Fig. 6). This age is the average of two reproducible K-Ar analyses (Table 1), made on a perfectly unaltered rock in macroscopic and microscopic views (Figs S1, S2), with a low negative LOI (-0.29 wt.%, Table 2) indicative of freshly erupted nephelinite. This Holocene age is further supported by the morphology of the lava flow filling the back of the modern fringing reef (T0, Fig. 6b). The construction of modern fringing reefs in the Indian ocean has initiated 8 – 9 ka ago due to the last post-glacial sea level rise (Camoin et al., 2004). The lava flow is thus younger than 9 ka, in consistency with its K-Ar age at 8 ± 2 ka. There are thus Holocene volcanic deposits on Mohéli, as on Grande Comore, Anjouan, and perhaps Mayotte (Zinke et al., 2003; Quidelleur et al., 2022).

Our geochronological results may also be used to constrain the timing and magnitude of vertical movements. Indeed, the radial islets south of Mohéli imply that the erosional valleys of the early volcano, filled at 3.3–3.1 Ma, then subsided after ~3 Ma and before the construction of the N110°E ridge (Fig. 6a). Drowned carbonate platforms T2 and T3 at 400–600 m depth on the SW and NE of Mohéli (Fig. 1b) confirm the subsidence of the N070°E structure at a rate greater than the growth rate capacity of coral reefs. Based on the depths of these drowned reefs, and after subtracting the depth at the base of the modern shelf (100–200 m), we calculate a long-term subsidence rate of 0.2–0.6 mm/yr in the ca. 1 Myrs period between Stages 1 and 2. Similar long-term subsidence rates have been found for volcanic edifices worldwide in various geodynamic settings (e.g., 0.25–0.39 mm/yr over 500 kyrs for Tahiti, Thomas et al., 2012; 0.2 mm/yr over 3 Myrs for the Kahouanne seamounts, Carey et al., 2020; 0.4 mm/yr over 125 kyrs in Les Saintes, Leclerc et al., 2014). In the case of Mohéli, however, this long-term subsidence rate must be considered as a very minimum, given the capacity of coral reefs to grow at rates of up to 7 mm/yr nearby in Mayotte (Camoin et al., 2004). Reef drowning must have been much more rapid than estimated by our long-term subsidence rate. Drowned carbonate platforms are also reported on the lower slopes of Mayotte at 400–800 m depth (Audru et al., 2006), the ages of which are unknown, and further work is obviously needed to compare the chronology of subsidence on the two islands in order to draw geodynamic inferences.

The modern carbonate insular shelf T1, less than 100 m-deep, is built on the slopes of the second stage N110°E ridge as well as on the slopes of the first stage N070°E axis (Fig. 1b). We therefore interpret T1 to be under construction since less than 2 Ma. This modern shelf indicates that, after sudden drowning between 3 and 2 Ma, subsidence halted or slowed down during the

volcano-tectonic Stage 2, allowing coral reef growth to catch up vertical movement. Using our age constraints, we calculate a long-term subsidence rate of less than 0.2 mm/yr since the beginning of Stage 2 ca. 2 Ma ago, which is about the sea-level-corrected subsidence rate calculated for Mayotte in the Holocene (Camoin et al., 2004).

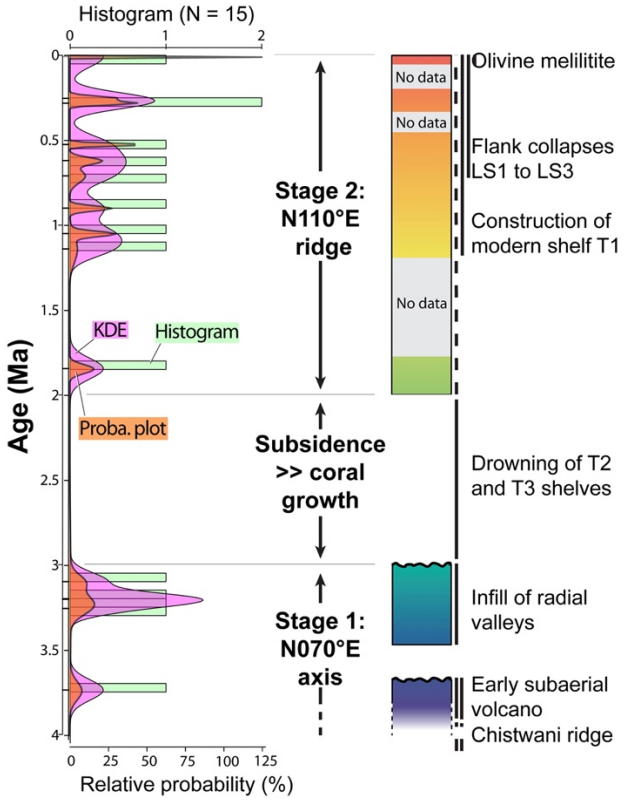

Figure 7: Chronostratigraphic chart of Mohéli and the Chistwani ridge based on criteria of relative chronology (geomorphology, unconformities, etc.) and on age frequency in three different representations (age-probability spectra after Deino and Potts, 1992; Kernel density estimation – KDE – at 0.05 Ma bin, and histogram at 0.05 Ma bin). Abbreviations T1 to T3 and LS1 to LS3 refer to structures shown in Figure 1b. Color chart is the same as in Figs 1 – 6.

5.3 Geochemical evolution of Mohéli's magmas

Major and trace elements show that the two volcano-tectonic stages identified above are characterized by two distinct major and trace element signatures of eruptive products (Figs 4, 5). The magmas emitted during Stage 1 (including MO 10, the only validated K-Ar whole-rock age of the first stage with major element data available) are moderately silica-undersaturated basalts and basanites (Fig. 3a), with mild enrichments in incompatible elements relative to primitive mantle (Fig. 4). These characteristics are similar to those of mafic magmas from the Karthala volcano in Grande Comore, Anjouan, and to the moderately undersaturated trend of Mayotte (Class et al., 1998; Pelleter et al., 2014; Bachèlery and Hémond, 2016). Stage 2, in contrast, is characterized by highly silica-undersaturated eruptive products (Fig. 3), with marked enrichments in incompatible elements compared to the first stage (Figs 4, 5). Sample RH-36 (Emerick and Duncan, 1983, 1982), the only validated whole-rock K-Ar age of Stage 2 with major and trace element analyses available (Späth et al., 1996), is a tephri-basanite sharing this enrichment in incompatible elements (Figs 3, 4, 5a-b). The volcanic seamount dredged by SMR3 is also a silica-undersaturated rock (Fig. 3), with trace-element signatures similar to those of the Stage 2 (Figs 4, 5). These compositional characteristics further confirm that the

volcanic cone dredged by SMR3 is a volcanic structure of the N110°E ridge, belonging to the volcano-tectonic Stage 2 of Mohéli.

The question arises about which melting processes are responsible for the geochemical diversity of Mohéli's magmas. Ratios such as Nb/U and Ce/Pb, which are insensitive to variable partial melting, are comparable to normal MORB/OIB (e.g. Rasoazanamparany et al., 2021, 2022) and do not show any variation with time (Fig. 5d-e). This suggests that the temporal enrichment in incompatible elements is not the result of increasing crust assimilation. Intermediate Ta/Th values (0.4-0.9), uncorrelated to rock ages (Fig. 5f), argue against a pure asthenospheric source and suggest the presence of metasomatic apatite and/or rutile (Farmer et al., 2020). Moreover, highly silica-undersaturated rocks from Mohéli, and in particular melilite-bearing lavas, display similar major and trace element characteristics to those described by Pelleter et al. (2014) for Mayotte, namely high CaO and/or P_2O_5 contents (Fig. 8a), strong enrichments in incompatible elements such as F, Ba, Sr, Nb, and relative enrichments in MREE with respect to the other mafic rocks (Figs 4, 8b). Mohéli's and Mayotte's olivine melilitites also share minor and trace element similarities with those of central and eastern Madagascar (Melluso et al., 2011; Mazzeo et al., 2021, and references therein), like K and Pb throughs (Fig. 8b). Following Pelleter et al. (2014) for Mayotte, and Mazzeo et al. (2021) for eastern Madagascar, we thus interpret Mohéli's undersaturated magmas as generated by very low partial melting of a peridotitic source located in the lithospheric mantle, enriched in highly incompatible elements by CO_2 metasomatism. As for Mayotte's melilitites and for one melilitite in northern Madagascar (Cucciniello et al., 2016), Mohéli's olivine melilitite is among the most enriched in P (1.15 wt.%) of worldwide melilitites (max 1.35 wt.% in Mayotte and 1.27 wt.% in Nyiragongo, Fig. 8a, see compilation by Mazzeo et al., 2021). For Mayotte, Pelleter et al. (2014) interpreted this geochemical feature as contribution of apatite ± dolomite in magmas, either from the partial melting source or by assimilation during melt ascent. CO_2 metasomatism, already evidenced beneath Grande Comore (Coltorti et al., 1999) and Mayotte (Pelleter et al., 2014; see Bachèlery and Hémond, 2016 for a review), and now found in Mohéli, is thus a general feature of magmas from the Comoros archipelago. It is also a general feature of Cenozoic and Recent magmas from northern Madagascar, suggesting analogies in mantle sources and/or enrichment processes, as recently proposed by Cucciniello et al. (2022).

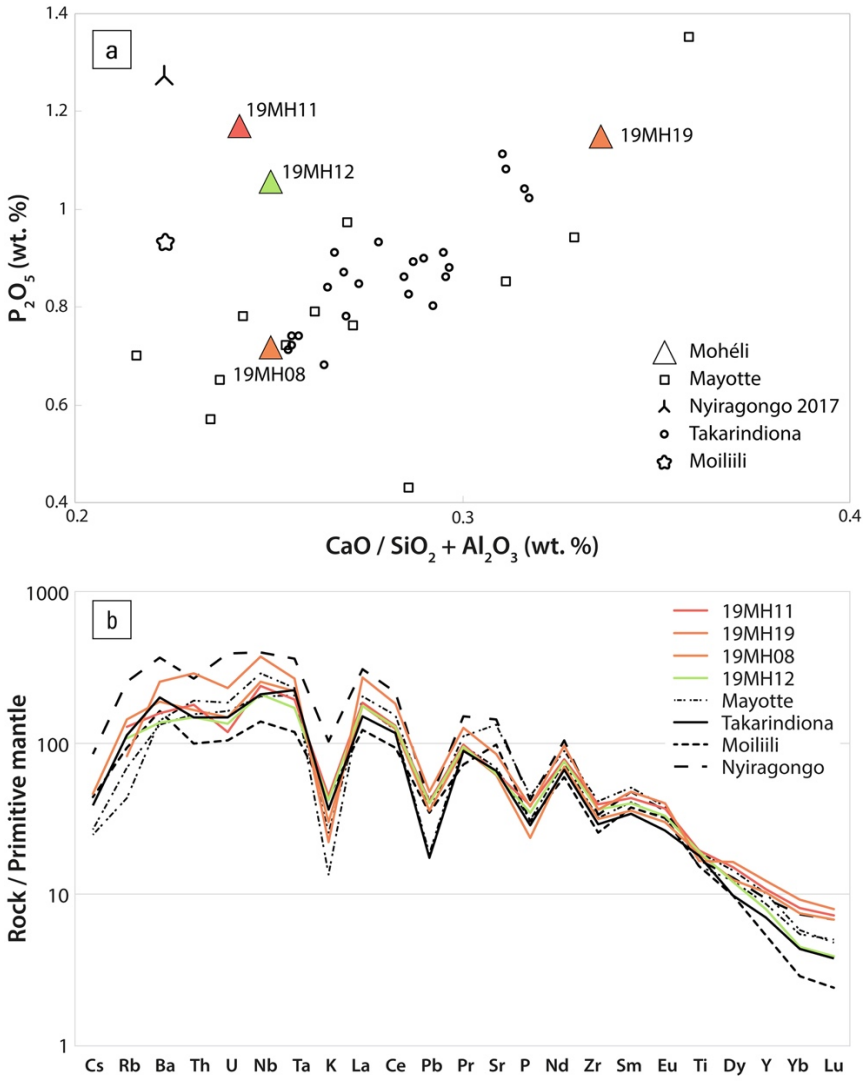

Figure 8: Comparison of highly silica-undersaturated lavas from Mohéli with those of Mayotte (Pelleter et al., 2014) and with melilitites worldwide (compilation from Mazzeo et al., 2021). a- P_2O_5 vs CaO/ (SiO_2 + Al_2O_3). b- Spider diagram. Color chart is the same as in Figs 1 – 7.

Despite the appearance of highly silica-undersaturated magmas, it is worth noting that the moderately undersaturated, basanitic magmas do not disappear in Stage 2, as shown by our sample 19MH07 (1.05 ± 0.02 Ma; Figs 4, 5). This situation is again reminiscent to that of Mayotte, where the moderately and highly silica-undersaturated melts coexisted in the same time intervals (Pelleter et al., 2014). Pelleter et al. (2014) interpreted this duality as reflecting variable partial melting of the same metasomatized lithospheric mantle. Applying this concept to Mohéli, age correlations with incompatible element concentration ratios (Figs 5b-c) suggest that partial melting of the lithosphere decreases over time from the N070°E axis to the N110°E ridge, even though batches of the initial magma are still erupting in the second stage.

5.4 Volcano-tectonic hazard assessment and geodynamic implications

The first implication of our study concerns the assessment of volcanic hazards in the Comoros archipelago. One of the most silica-undersaturated samples – the 19MH11 olivine nephelinite, is also the youngest dated lava flow (8 ± 2 ka; Fig. 3), consistent with its morphology younger than 9 ka (Fig. 6b). Holocene volcanic activity has recently been identified on Anjouan

(Quidelleur et al., 2022), and present-day activity occurs on Grande Comore and offshore Mayotte (Feuillet et al., 2021). Following the definition of the Smithsonian Global Volcanism Program, our discovery of Holocene volcano-tectonic activity <10 ka on Mohéli implies that all the islands of the archipelago must be considered as active in any assessment of volcanic hazard in the area. This finding should be kept in mind when interpreting the origin of volcanic deposits in the northern Mozambique channel. For instance, Zinke et al. (2003) described ash layers in cores of coral platforms in Mayotte dated between 7 and 4 ka. Many authors have attributed it to the latest volcanic activity of Petite Terre in Mayotte (e.g., Nehlig et al., 2013). However, that is called into question by a new study focused on the explosive phonolitic volcanism of Petite-Terre suggesting that it may have occurred 25 ka ago or earlier (Lacombe et al., 2023). In the absence of systematic chemical analyses, these ash layers found in cores could as well come from Grande Comore, Mohéli, or Anjouan. Care should be taken to include compositional constraints to assess the source of tephras anywhere in the Comoros archipelago.

Another volcano-tectonic implication of our study is related to the destabilization history of Mohéli's edifice. Tzevahirtzian et al. (2021) described two large (>20 km-long) collapse scars in the modern shelf T1, with up to 0.5 km^3 associated debris avalanche deposits on the southern slopes of Mohéli (Fig. 1). A smaller (<5 km-long) collapse scar is also described at the NE tip of T1, with debris flows or avalanche deposits partially covering the drowned platform T3 (Fig. 1b). Because all these flank collapses affected T1, they must be more recent than the main construction of the N110°E ridge, i.e., younger than ca. 1 Ma. These events should be put in the perspective of other flank collapses occurring on nearby volcano-tectonic structures. For instance, based on their new radiometric dating, Quidelleur et al. (2022) estimated the major collapses of the northern and southern slopes of Anjouan to have occurred after 0.9 Ma. Our results imply that at least two additional flank collapses occurred during the same time interval nearby on Mohéli, with the possibility that all these events might be chronologically or even genetically related. Destabilizations have also been evidenced on the slopes of Mayotte (Audru et al., 2006; Thinon et al., 2022), but their timing relative to Mohéli's and Anjouan's events is yet to be established.

By providing new age constraints on the volcano-tectonic history of Mohéli, our work also asks an important question: Why did Mohéli's volcano-tectonics shift from a N070°E structure emitting moderately silica-undersaturated magmas before 3 Ma, to a N110°E ridge emitting both highly silica-undersaturated and moderately-undersaturated magmas after 2 Ma? If, as proposed by Famin et al. (2020), the Comoros archipelago represents a dextral strike-slip boundary between the Somali and Lwandle plates, then the kinematics of this boundary seems to have changed from ≥3 Ma to ≤2 Ma in the Mohéli area. According to plate motion reconstructions from the spreading of the Southwest Indian Ridge, the Lwandle/Somali relative motion did not experience significant variation during this period (DeMets et al., 2021). Thus, the cause of this kinematic change has to be searched in relation to magmatic processes and the decrease of lithosphere partial melting. Further geochronological and geochemical work is needed to elucidate this question, at the broader scale of the Comoros province, encompassing the many newly discovered seamounts in the area (Thinon et al., 2022).

6. Conclusion

Our new K-Ar ages obtained by the Cassignol-Gillot approach on groundmass, combined with major and trace element whole-rock analyses, suggest that the volcano-tectonics of Mohéli has one of the most protracted histories among the islands of the Comoros archipelago. This history includes a first stage with the emersion of an early volcano and the activity of a submarine ridge

along a N070°E axis from before 3.8 Ma to ca. 3 Ma. This first volcano-tectonic Stage 1 was followed by ~1 Myrs of repose and increased subsidence of the island (≥0.2 mm/yr), causing the drowning of carbonate shelves. Then, a Stage 2 of submarine and subaerial volcanic activity resumed from ca. 2 Ma to Holocene times along a N110°E ridge, shaping the present-day morphology of the island and supporting the modern shelf. This two-stage shift of volcano-tectonics is accompanied by a chemical evolution of emitted magmas, from moderately silica-undersaturated and incompatible-element-enriched in the first stage, to the predominance of highly silica undersaturated and incompatible-element-enriched products in the second stage. The chemical characteristics of magmas and their evolution suggest that melts originate from a CO_2-metasomatized lithospheric mantle, with decreasing partial melting over time. One of the most silica-undersaturated products, a melilite-bearing lava, revealed the youngest age of 8 ± 2 ka. This Holocene age implies a possible volcanic hazard in Mohéli Island, and thus a potential resumption of volcanism anywhere in the Comoros archipelago. The report of melilite-bearing lavas in Mohéli further supports the hypothesis that volcanism in the Comoros archipelago shares similarities in magmas sources and ascent processes with the Cenozoic volcanism of northern and eastern Madagascar.

Acknowledgments

This research is part of A. Rusquet's PhD, funded by the French Agence Nationale de la Recherche (ANR) in the framework of the ANR COYOTES project number ANR-19-CE31-0018 (https://anr.fr/Projet-ANR-19-CE31-0018). We thank the SISMAORE and COYOTES teams for discussions, onboard processing of the geophysical data and help for the rock sampling, in particular Carole Berthod and Julien Bernard. This research was also funded by the MAYVOLTE grant from the Institut des Sciences de l'Univers (INSU), Centre National de la Recherche Scientifique (CNRS). We thank the Parc National Marin de Mohéli and his head Lailina Daniel for logistical support during the fieldwork. We also thank Choubaikat Mohamed Moutuou for her help with dating of sample 19MH19.

665 **Table captions**

666

667 **Table 1:** New K-Ar ages performed on groundmass separates. Column headings indicate
668 sample names; latitude and longitude in decimal degrees; potassium (K) concentration in
669 percent; concentration of radiogenic argon (^{40}Ar*) in percent; concentration of ^{40}Ar* $\times 10^{11}$ in
670 number of atoms per gram; age (in Ma); 1σ uncertainty (Un., in Ma); weighted mean age (in
671 Ma); 1σ weighted mean uncertainty (in Ma).

Sample	Latitude (S)	Longitude (E)	K (%)	^{40}Ar* (%)	^{40}Ar* (10^{11} at/g)	Age (Ma)	Un. (Ma)	**Mean age (Ma)**	**± 1 σ (Ma)**
SMR4A	44.09840	-12.28448	1.080	49.45	42.121	3.729	0.053	**3.738**	**0.054**
Duplicate				39.50	42.348	3.749	0.054		
19MH03	43.77262	-12.36906	0.922	57.84	31.460	3.264	0.046	**3.258**	**0.046**
Duplicate				58.66	31.355	3.253	0.046		
19MH04	43.84465	-12.37112	1.134	16.29	6.2448	0.527	0.008	**0.525**	**0.008**
Duplicate				17.20	6.2025	0.524	0.008		
19MH07	43.84292	-12.34042	1.277	35.03	14.096	1.056	0.015	**1.050**	**0.015**
Duplicate				44.83	13.942	1.045	0.015		
19MH08	43.78596	-12.32026	1.088	2.88	3.3024	0.29	0.011	**0.282**	**0.010**
Duplicate				3.18	3.1256	0.275	0.009		
19MH11	43.76331	-12.29747	2.037	0.34	0.17876	0.008	0.002	**0.008**	**0.002**
Duplicate				0.30	0.14158	0.007	0.002		
19MH12	43.65196	-12.25466	1.538	45.02	29.475	1.834	0.026	**1.845**	**0.026**
Duplicate				47.91	29.812	1.855	0.027		
19MH15	43.70800	-12.41180	1.106	61.50	35.846	3.099	0.044	**3.100**	**0.044**
Duplicate				56.48	35.866	3.101	0.044		
19MH17	43.66015	-12.40251	1.203	47.26	40.199	3.197	0.046	**3.204**	**0.046**
Duplicate				47.39	40.369	3.211	0.046		
19MH19	43.67247	-12.35664	1.150	1.89	3.0352	0.253	0.014	**0.253**	**0.013**
Duplicate				2.28	3.0391	0.253	0.012		
19MH20	43.64081	-12.29331	1.470	9.73	13.934	0.907	0.016	**0.900**	**0.015**
Duplicate				12.08	13.743	0.895	0.015		

672

673 **Table 2:** Major (in percent) and trace element (in ppm) compositions of whole-rock samples.
674 L.O.I.: loss on ignition.

Sample	SMR3A	SMR4A	19MH03	19MH04	19MH07	19MH08	19MH11	19MH12	19MH15	19MH17	19MH19	19MH20
(wt.%)												
SiO_2	41.11	44.17	45.54	41.05	45.39	39.13	39.67	39.24	44.20	44.88	36.87	42.28
TiO_2	3.28	2.45	2.84	2.58	2.74	2.97	3.12	3.03	2.48	2.52	2.66	2.50
Al_2O_3	13.58	11.86	14.11	12.16	13.68	11.57	10.91	10.55	11.61	11.54	11.02	12.81
Fe_2O_3	14.30	13.12	14.27	14.62	14.40	14.90	15.36	15.91	13.28	13.97	15.39	14.75
MnO	0.242	0.196	0.192	0.225	0.183	0.232	0.254	0.210	0.164	0.186	0.302	0.233
MgO	4.02	9.19	5.68	9.99	8.23	11.45	10.66	11.67	10.77	12.52	9.82	9.51
CaO	8.43	11.67	11.59	11.98	9.83	12.72	12.28	12.49	11.67	10.29	16.10	11.55
Na_2O	5.19	3.23	2.79	3.87	3.20	3.35	4.60	4.80	1.87	2.35	3.23	3.98
K_2O	2.64	1.26	1.08	1.07	1.27	1.37	2.05	1.92	0.97	1.11	1.02	1.47
P_2O_5	1.56	0.63	0.44	0.94	0.52	0.71	1.17	1.05	0.62	0.42	1.15	0.86
LOI	4.94	1.13	1.06	1.62	0.31	1.50	-0.29	-0.11	2.87	0.68	2.40	0.38
Total	99.29	98.91	99.59	100.09	99.75	99.90	99.79	100.70	100.49	100.47	99.96	100.33
(ppm)												
Be	4.92	2.74	1.82	2.40	1.60	2.96	3.11	3.62	2.07	1.69	3.47	3.01
Sr	1414	623	432	756	501	982	985	985	966	389	1313	845
Y	60.4	35.0	25.2	31.1	24.6	34.8	36.7	27.0	25.5	20.7	41.7	35.8
Zr	450	234	208	247	200	265	331	307	202	195	308	282
Mo	6.00	4.71	1.80	4.66	1.74	3.89	3.75	5.36	2.53	1.63	0.76	6.19
Cs	0.66	0.34				0.73						
Ba	891	385	322	761	436	952	800	693	382	295	1289	758
La	106	45.8	33.4	76.8	37.9	89.4	94.7	90.3	51.8	30.9	139	82.0
Ce	200	88.2	67.3	138	73.8	168	176	172	100	62.3	244	149
Pr	25.0	10.9	8.25	15.1	8.73	18.7	19.8	19.4	11.8	7.54	25.9	16.1
Nd	98.8	44.1	34.8	58.7	36.2	69.5	78.2	75.8	47.6	31.5	95.9	61.4
Sm	18.3	8.88	7.11	10.4	7.34	11.6	14.0	13.1	9.01	6.28	15.5	10.7
Eu	5.85	2.89	2.42	3.47	2.54	3.68	4.55	4.10	2.98	2.12	4.96	3.52
Gd	17.2	8.72	7.06	10.4	7.44	10.9	13.3	12.5	8.75	6.34	14.7	11.0
Tb	2.28	1.24	1.06	1.41	1.08	1.41	1.77	1.56	1.21	0.92	1.89	1.49
Dy	10.9	6.41	5.44	6.80	5.40	6.70	8.22	6.54	5.79	4.59	8.81	7.12
Ho	1.97	1.17	1.01	1.22	0.97	1.21	1.45	1.04	1.01	0.84	1.58	1.31
Er	4.69	2.89	2.52	2.95	2.35	2.96	3.42	2.17	2.39	2.02	3.82	3.18
Tm	0.63	0.41	0.35	0.40	0.32	0.42	0.46	0.26	0.32	0.28	0.52	0.44
Yb	3.87	2.47	2.17	2.45	1.97	2.57	2.83	1.55	1.96	1.70	3.18	2.74
Lu	0.54	0.35	0.30	0.34	0.27	0.37	0.39	0.21	0.28	0.23	0.43	0.39
Hf	11.5	6.41	4.95	5.12	4.65	7.04	6.59	6.03	4.57	4.53	6.10	5.31
W	2.71	1.41	0.51	1.79	0.63	0.73	1.61	1.76	0.58	0.59	0.42	3.25
Pb	6.27	4.49	2.92	6.20	2.39	5.19	6.01	5.76	3.54	2.70	6.93	5.37
Th	9.16	4.27	3.49	10.3	3.99	10.4	11.3	9.30	5.46	3.41	18.0	10.6
U	2.38	1.13	0.86	2.80	0.82	2.58	2.07	2.32	1.40	0.90	4.00	2.39
Li	23.9	11.0				11.0						
Sc	14.2	39.6				34.1						
V	152	388	317	235	237	387	238	263	269	257	258	240
Cr	3.27	713	29.7	284	214	463	357	522	567	443	337	308
Co	34.6	76.3	47.7	55.6	58.2	80.4	56.9	68.5	61.2	64.5	54.9	59.1
Ni	9.62	258	86.2	184	183	273	215	276	278	354	160	198
Cu	20.8	130	111	65.4	62.7	96.9	57.6	79.1	90.7	89.0	68.5	63.8
Zn	205	146	127	130	136	143	154	177	125	121	155	146
Ga	24.6	23.5				21.3						
Rb	66.7	35.7	22.3	19.8	30.3	65.6	58.5	49.0	32.4	23.2	37.6	49.4
Nb	116	47.6	45.8	88.3	50.2	118	110	96.3	51.2	42.3	172	94.4
Ta	6.24	2.70	2.79	4.86	2.94	6.72	5.89	5.18	2.68	2.58	8.14	4.91

675

676

677 **Supplementary Material**

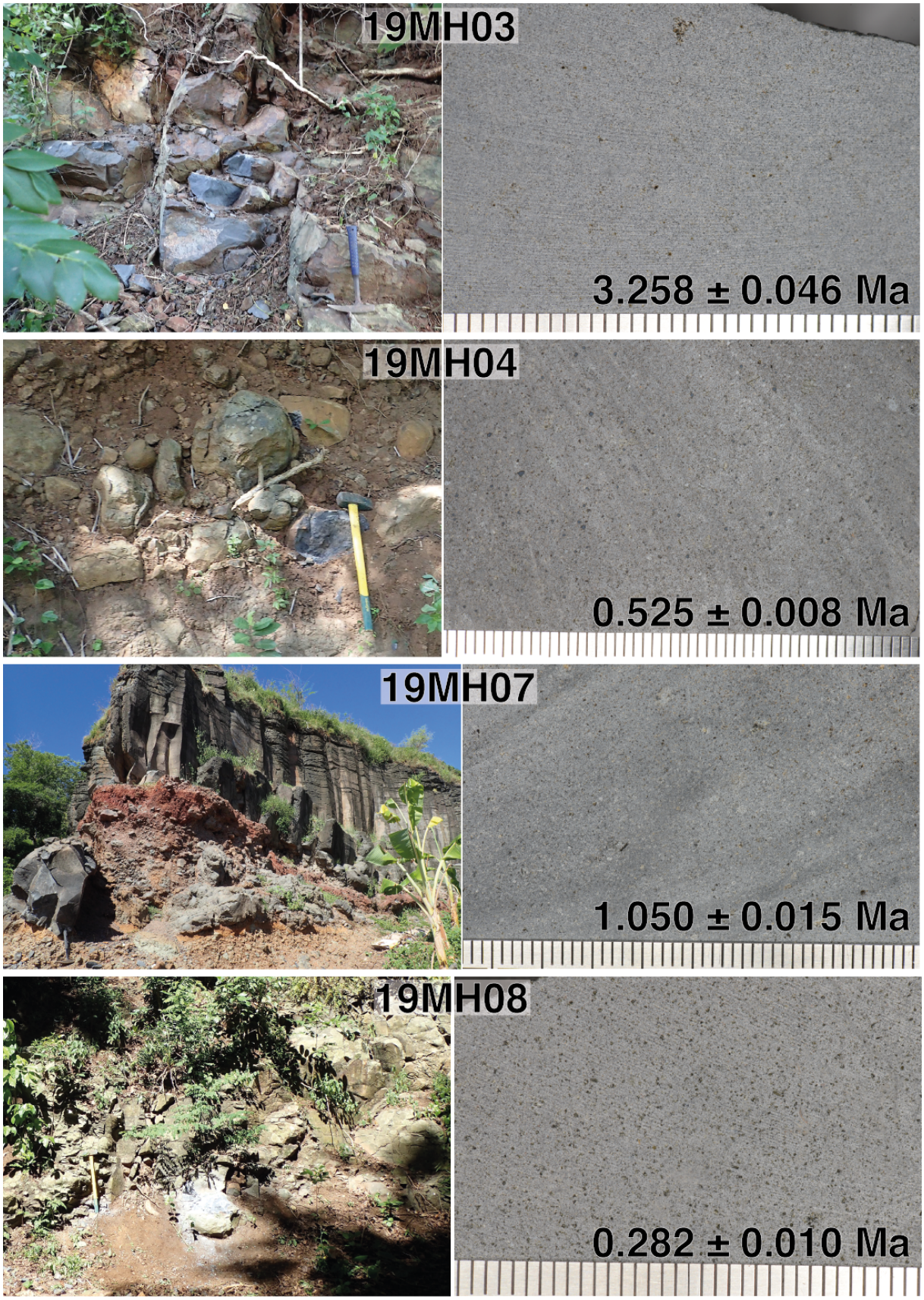

Figure S1: Outcrop and/or hand specimen pictures of the rocks sampled in Mohéli, and corresponding macroscopic pictures of saw-cut slabs with their K-Ar age on groundmass.

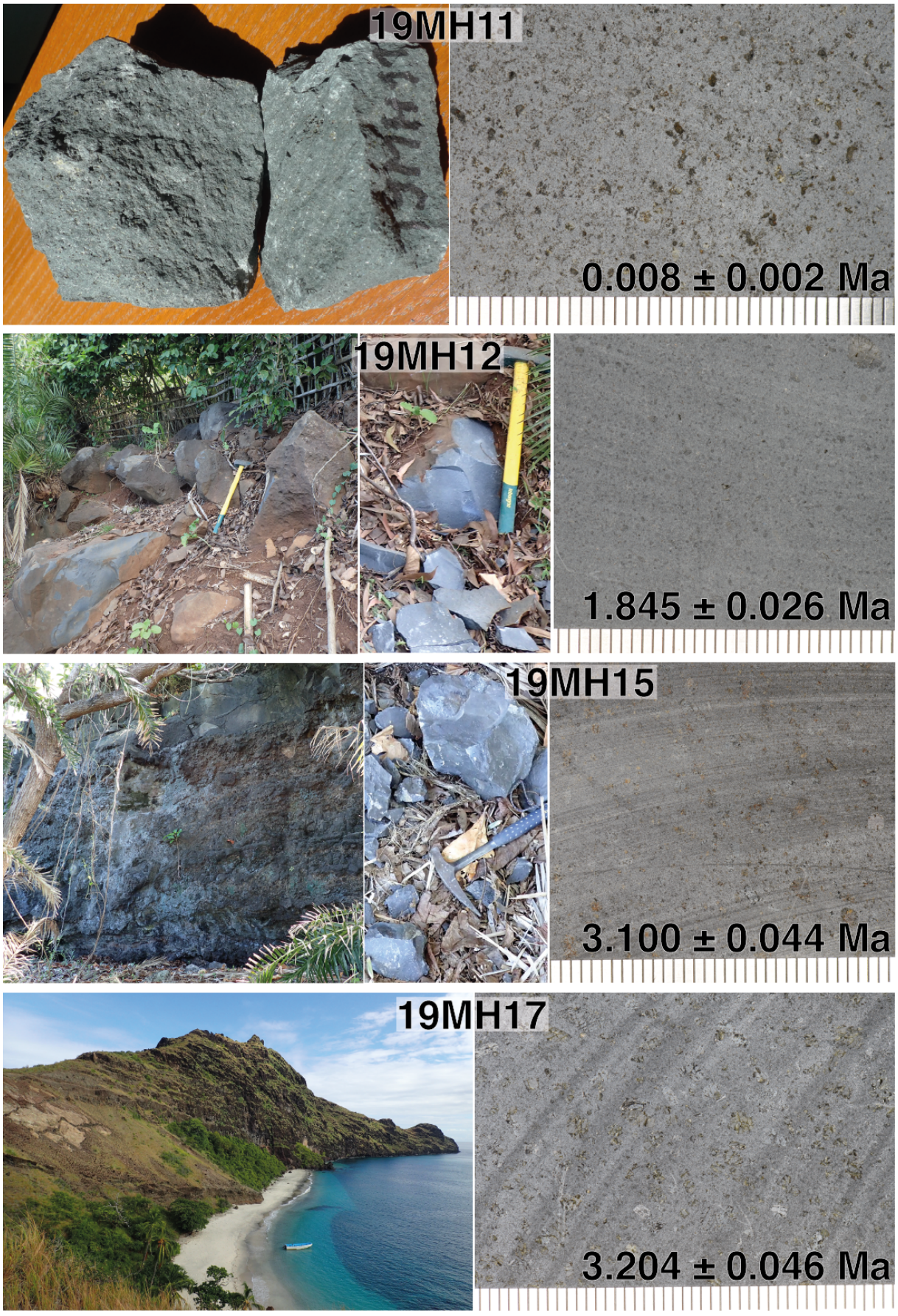

Figure S1 (continued)

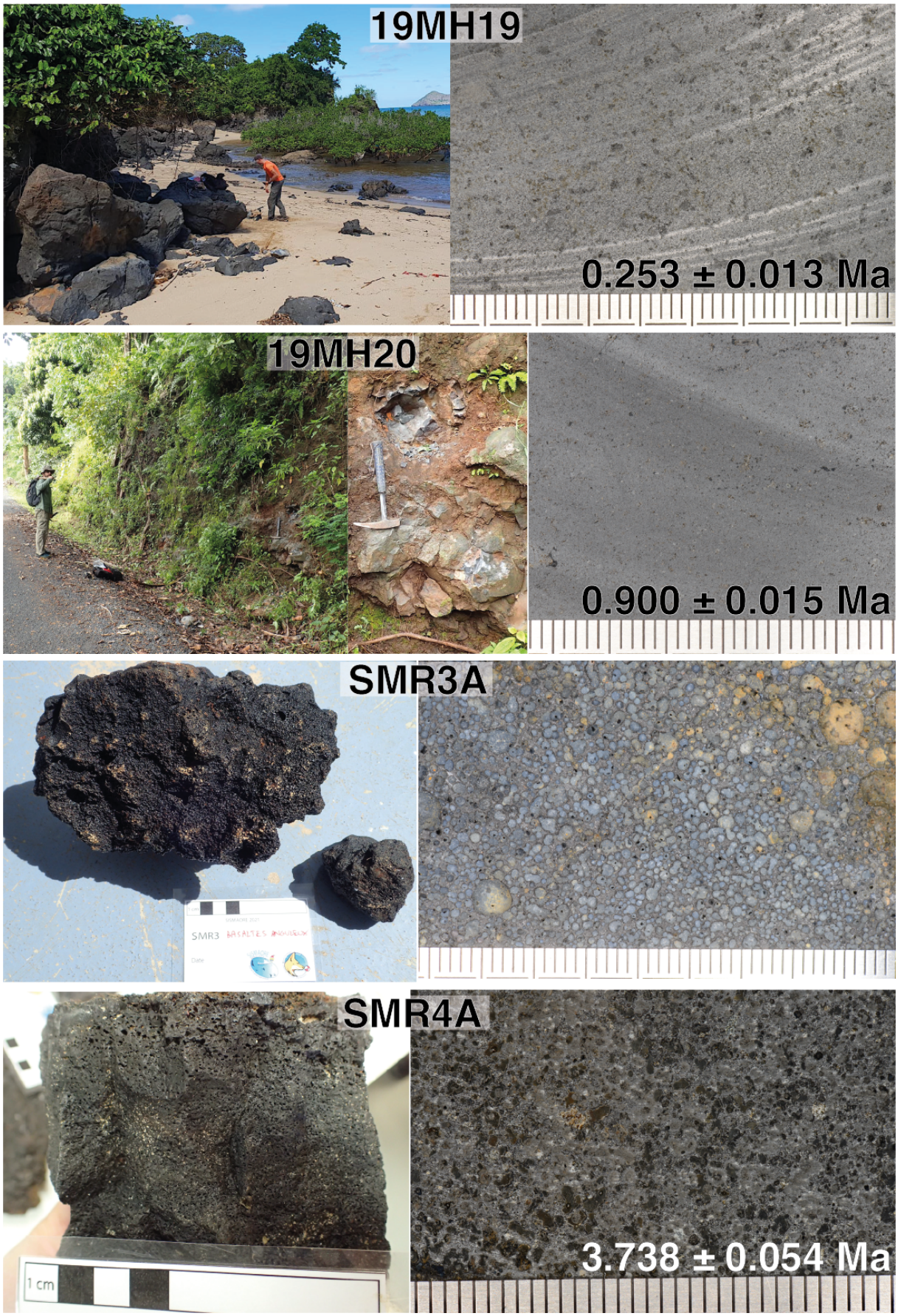

Figure S1 (continued)

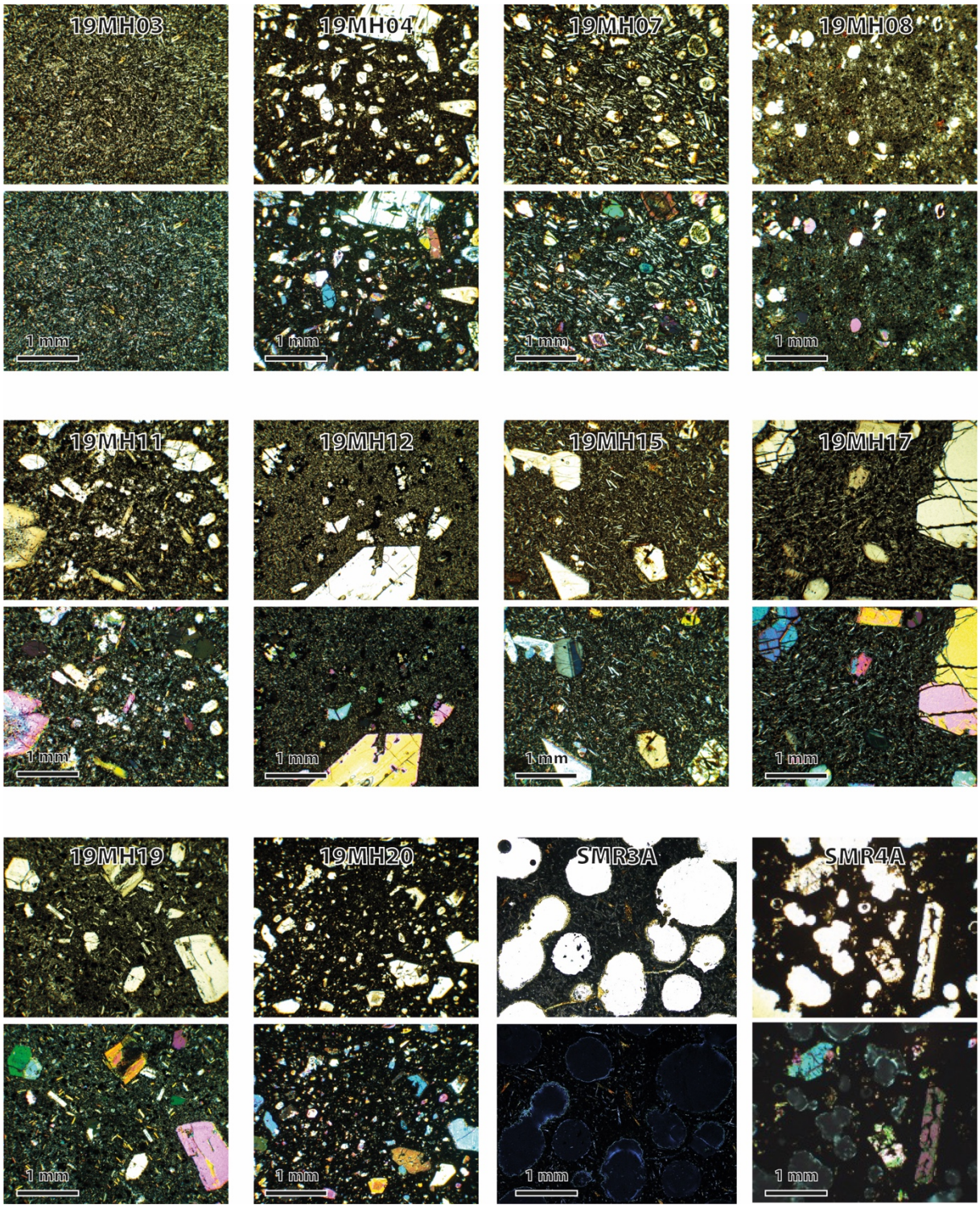

Figure S2: Optical microphotographs of submarine and subaerial samples used for K-Ar dating. Top: plane-polarized light; bottom: cross-polarized light.

References

Audru, J.-C., Guennoc, P., Thinon, I., Abellard, O., 2006. Bathymay : la structure sous-marine de Mayotte révélée par l'imagerie multifaisceaux. Comptes Rendus Geosci. 338, 1240–1249. https://doi.org/10.1016/j.crte.2006.07.010

Bablon, M., Quidelleur, X., Samaniego, P., Le Pennec, J.-L., Audin, L., Jomard, H., Baize, S., Liorzou, C., Hidalgo, S., Alvarado, A., 2019. Interactions between volcanism and geodynamics in the southern termination of the Ecuadorian arc. Tectonophysics 751, 54–72. https://doi.org/10.1016/j.tecto.2018.12.010

Bachèlery, P., Hémond, C., 2016. Geochemical and Petrological Aspects of Karthala Volcano, in: Bachelery, P., Lenat, J.-F., Di Muro, A., Michon, L. (Eds.), Active Volcanoes of the Southwest Indian Ocean, Active Volcanoes of the World. Springer Berlin Heidelberg, Berlin, Heidelberg, pp. 367–384. https://doi.org/10.1007/978-3-642-31395-0_23

Berthod, C., Médard, E., Bachèlery, P., Gurioli, L., Di Muro, A., Peltier, A., Komorowski, J.-C., Benbakkar, M., Devidal, J.-L., Langlade, J., Besson, P., Boudon, G., Rose-Koga, E., Deplus, C., Le Friant, A., Bickert, M., Nowak, S., Thinon, I., Burckel, P., Hidalgo, S., Kaliwoda, M., Jorry, S.J., Fouquet, Y., Feuillet, N., 2021a. The 2018-ongoing Mayotte submarine eruption: Magma migration imaged by petrological monitoring. Earth Planet. Sci. Lett. 571, 117085. https://doi.org/10.1016/j.epsl.2021.117085

Berthod, C., Zaragosi, S., Famin, V., 2021b. SCRATCH cruise, R/V Marion Dufresne. https://doi.org/10.17600/18002274

Blard, P., Lave, J., Pik, R., Quidelleur, X., Bourles, D., Kieffer, G., 2005. Fossil cosmogenic He record from K–Ar dated basaltic flows of Mount Etna volcano (Sicily, 38°N): Evaluation of a new paleoaltimeter. Earth Planet. Sci. Lett. 236, 613–631. https://doi.org/10.1016/j.epsl.2005.05.028

Camoin, G.F., Montaggioni, L.F., Braithwaite, C.J.R., 2004. Late glacial to post glacial sea levels in the Western Indian Ocean. Mar. Geol. 206, 119–146. https://doi.org/10.1016/j.margeo.2004.02.003

Carey, S., Sparks, R.S.J., Tucker, M.E., Li, T., Robinson, L., Watt, S.F.L., Gee, M., Hastie, A., Barfod, D.N., Stinton, A., Leng, M., Raineault, N., Ballard, R.D., 2020. The polygenetic Kahouanne Seamounts in the northern Lesser Antilles island arc: Evidence for large-scale volcanic island subsidence. Mar. Geol. 419, 106046. https://doi.org/10.1016/j.margeo.2019.106046

Carignan, J., Hild, P., Mevelle, G., Morel, J., Yeghicheyan, D., 2001. Routine Analyses of Trace Elements in Geological Samples using Flow Injection and Low Pressure On-Line Liquid Chromatography Coupled to ICP-MS: A Study of Geochemical Reference Materials BR, DR-N, UB-N, AN-G and GH. Geostand. Geoanalytical Res. 25, 187–198. https://doi.org/10.1111/j.1751-908X.2001.tb00595.x

Cassignol, C., Gillot, P.-Y., 1982. Range and effectiveness of unspiked potassium-argon dating: experimental groundwork and applications, in: Numerical Dating in Stratigraphy. Wiley, pp. 159–179.

Class, C., Goldstein, S., Stute, M., Kurz, M., Schlosser, P., 2005. Grand Comore Island: A well-constrained "low 3He/4He" mantle plume. Earth Planet. Sci. Lett. 233, 391–409. https://doi.org/10.1016/j.epsl.2005.02.029

Class, C., Goldstein, S.L., 1997. Plume-lithosphere interactions in the ocean basins: constraints from the source mineralogy. Earth Planet. Sci. Lett. 150, 245–260. https://doi.org/10.1016/S0012-821X(97)00089-7

Class, C., Goldstein, S.L., Altherr, R., Bachèlery, P., 1998. The Process of Plume–Lithosphere Interactions in the Ocean Basins - the Case of Grande Comore. J. Petrol. 39, 881–903. https://doi.org/10.1093/petroj/39.5.881

Claude-Ivanaj, C., Bourdon, B., Allègre, C.J., 1998. Ra–Th–Sr isotope systematics in Grande Comore Island: a case study of plume–lithosphere interaction. Earth Planet. Sci. Lett. 164, 99–117. https://doi.org/10.1016/S0012-821X(98)00195-2
Coltorti, M., Bonadiman, C., Hinton, R.W., Siena, F., Upton, B.G.J., 1999. Carbonatite Metasomatism of the Oceanic Upper Mantle: Evidence from Clinopyroxenes and Glasses in Ultramafic Xenoliths of Grande Comore, Indian Ocean. J. Petrol. 40, 133–165. https://doi.org/10.1093/petroj/40.1.133
Cucciniello, C., Grifa, C., de'Gennaro, R., Franciosi, L., Rocco, I., Morra, V., Melluso, L., 2022. Alkaline rocks of the Bobaomby volcanic field point to a petrogenetic link between Comoros and northern Madagascar lithosphere. Int. J. Earth Sci. https://doi.org/10.1007/s00531-022-02251-9
Cucciniello, C., Tucker, R.D., Jourdan, F., Melluso, L., Morra, V., 2016. The age and petrogenesis of alkaline magmatism in the Ampasindava Peninsula and Nosy Be archipelago, northern Madagascar. Mineral. Petrol. 110, 309–331. https://doi.org/10.1007/s00710-015-0387-1
Dasgupta, R., Hirschmann, M.M., Smith, N.D., 2007. Partial Melting Experiments of Peridotite + CO2 at 3 GPa and Genesis of Alkalic Ocean Island Basalts. J. Petrol. 48, 2093–2124. https://doi.org/10.1093/petrology/egm053
De Saint Ours, J., 1960. Etudes géologiques dans l'extrême nord de Madagascar et l'archipel des Comores. Service géologique.
Deino, A., Potts, R., 1992. Age-probability spectra for examination of single-crystal dating results: Examples from Olorgesailie, southern Kenya Rift. Quat. Int. 13–14, 47–53. https://doi.org/10.1016/1040-6182(92)90009-Q
DeMets, C., Merkouriev, S., Sauter, D., 2021. High resolution reconstructions of the Southwest Indian Ridge, 52 Ma to present: implications for the breakup and absolute motion of the Africa plate. Geophys. J. Int. 226, 1461–1497. https://doi.org/10.1093/gji/ggab107
Deniel, C., 1998. Geochemical and isotopic (Sr, Nd, Pb) evidence for plume–lithosphere interactions in the genesis of Grande Comore magmas (Indian Ocean). Chem. Geol. 144, 281–303. https://doi.org/10.1016/S0009-2541(97)00139-3
Dofal, A., Michon, L., Fontaine, F.R., Rindraharisaona, E., Barruol, G., Tkalčić, H., 2022. Imaging the lithospheric structure and plumbing system below the Mayotte volcanic zone. Comptes Rendus Géoscience 354, 47–64. https://doi.org/10.5802/crgeos.190
Duncan, R.A., Hogan, L.G., 1994. Radiometric dating of young MORB using the ^{40}Ar-^{39}Ar incremental heating method. Geophys. Res. Lett. 21, 1927–1930. https://doi.org/10.1029/94GL01375
Emerick, C.M., Duncan, R.A., 1983. Errata. Earth Planet. Sci. Lett. 62, 439. https://doi.org/10.1016/0012-821X(83)90014-6
Emerick, C.M., Duncan, R.A., 1982. Age progressive volcanism in the Comores Archipelago, western Indian Ocean and implications for Somali plate tectonics. Earth Planet. Sci. Lett. 60, 415–428. https://doi.org/10.1016/0012-821X(82)90077-2
Esson, J., Flower, M.F.J., Strong, D.F., Upton, B.G.J., Wadsworth, W.J., 1970. Geology of the Comores Archipelago, Western Indian Ocean. Geol. Mag. 107, 549–557. https://doi.org/10.1017/S0016756800058647
Famin, V., Michon, L., Bourhane, A., 2020. The Comoros archipelago: a right-lateral transform boundary between the Somalia and Lwandle plates. Tectonophysics 789, 228539. https://doi.org/10.1016/j.tecto.2020.228539
Farmer, G.L., Fritz, D.E., Glazner, A.F., 2020. Identifying Metasomatized Continental Lithospheric Mantle Involvement in Cenozoic Magmatism From Ta/Th Values, Southwestern North America. Geochem. Geophys. Geosystems 21. https://doi.org/10.1029/2019GC008499
Feuillet, N., Jorry, S., Crawford, W.C., Deplus, C., Thinon, I., Jacques, E., Saurel, J.M.,

796 Lemoine, A., Paquet, F., Satriano, C., Aiken, C., Foix, O., Kowalski, P., Laurent, A., Rinnert,
797 E., Cathalot, C., Donval, J.-P., Guyader, V., Gaillot, A., Scalabrin, C., Moreira, M., Peltier,
798 A., Beauducel, F., Grandin, R., Ballu, V., Daniel, R., Pelleau, P., Gomez, J., Besançon, S.,
799 Geli, L., Bernard, P., Bachelery, P., Fouquet, Y., Bertil, D., Lemarchand, A., Van der Woerd,
800 J., 2021. Birth of a large volcanic edifice offshore Mayotte via lithosphere-scale dyke
801 intrusion. Nat. Geosci. 14, 787–795. https://doi.org/10.1038/s41561-021-00809-x
802 Flower, M.F.J., 1973. Evolution of basaltic and differentiated lavas from Anjouan, Comores
803 Archipelago. Contrib. Mineral. Petrol. 38, 237–260. https://doi.org/10.1007/BF00374768
804 Flower, M.F.J., 1971. Rare earth element distribution in lavas and ultramafic xenoliths from
805 the Comores Archipelago, Western Indian Ocean. Contrib. Mineral. Petrol. 31, 335–346.
806 https://doi.org/10.1007/BF00371153
807 Flower, M.F.J., Strong, D.F., 1969. The significance of sandstone inclusions in lavas of the
808 comores archipelago. Earth Planet. Sci. Lett. 7, 47–50. https://doi.org/10.1016/0012-
809 821X(69)90010-7
810 Fuhrmann, U., Lippolt, H.J., Hess, J.C., 1987. Examination of some proposed K-Ar standards:
811 analyses and conventional K-Ar data. Chem. Geol. Isot. Geosci. Sect. 66, 41–51.
812 https://doi.org/10.1016/0168-9622(87)90027-3
813 Germa, A., Quidelleur, X., Labanieh, S., Lahitte, P., Chauvel, C., 2010. The eruptive history
814 of Morne Jacob volcano (Martinique Island, French West Indies): Geochronology,
815 geomorphology and geochemistry of the earliest volcanism in the recent Lesser Antilles arc.
816 J. Volcanol. Geotherm. Res. 198, 297–310. https://doi.org/10.1016/j.jvolgeores.2010.09.013
817 Gertisser, R., Charbonnier, S.J., Keller, J., Quidelleur, X., 2012. The geological evolution of
818 Merapi volcano, Central Java, Indonesia. Bull. Volcanol. 74, 1213–1233.
819 https://doi.org/10.1007/s00445-012-0591-3
820 Gillot, P.-Y., Cornette, Y., 1986. The Cassignol technique for potassium—Argon dating,
821 precision and accuracy: Examples from the Late Pleistocene to Recent volcanics from
822 southern Italy. Chem. Geol. Isot. Geosci. Sect. 59, 205–222. https://doi.org/10.1016/0168-
823 9622(86)90072-2
824 Gillot, P.-Y., Cornette, Y., Max, N., Floris, B., 1992. Two reference materials, trachytes
825 MDO-G and ISH-G, for argon dating (K-Ar and 40Ar/39Ar) of Pleistocene and Holocene
826 rocks. Geostand. Geoanalytical Res. 16, 55–60. https://doi.org/10.1111/j.1751-
827 908X.1992.tb00487.x
828 Gillot, P.-Y., Hildenbrand, A., Lefèvre, J.-C., Livadie, C.A., 2006. The K/Ar dating method:
829 principle, analytical techniques, and application to Holocene volcanic eruptions in southern
830 Italy. Acta Vulcanol. 18, 55–66.
831 Gudfinnsson, G.H., Presnall, D.C., 2005. Continuous Gradations among Primary
832 Carbonatitic, Kimberlitic, Melilititic, Basaltic, Picritic, and Komatiitic Melts in Equilibrium
833 with Garnet Lherzolite at 3–8 GPa. J. Petrol. 46, 1645–1659.
834 https://doi.org/10.1093/petrology/egi029
835 Hajash, A., Armstrong, R.L., 1972. Paleomagnetic and radiometric evidence for the age of the
836 Comores Islands, west central Indian Ocean. Earth Planet. Sci. Lett. 16, 231–236.
837 https://doi.org/10.1016/0012-821X(72)90195-1
838 Henri, M., Quidelleur, X., Le Friant, A., Komorowski, J.-C., Escartín, J., Deplus, C., Mevel,
839 C., 2022. K-Ar Geochronology and geochemistry of underwater lava samples from the
840 Subsaintes cruise offshore Les Saintes (Guadeloupe): Insights for the Lesser Antilles arc
841 magmatism. Mar. Geol. 450, 106862. https://doi.org/10.1016/j.margeo.2022.106862
842 Hess, J.C., Lippolt, H.J., 1994. Compilation of K/Ar measurements on HD-B1 standard
843 biotite; 1994 status report, in: Phanerozoic Time Scale. Bulletin de Liaison et d'information,
844 IUGS Subcommission, Geochronology, pp. 19–23.
845 Hirose, K., 1997. Partial melt compositions of carbonated peridotite at 3 GPa and role of CO_2

in alkali-basalt magma generation. Geophys. Res. Lett. 24, 2837–2840. https://doi.org/10.1029/97GL02956
Hofmann, A.W., 1997. Mantle geochemistry: the message from oceanic volcanism. Nature 385, 219–229. https://doi.org/10.1038/385219a0
Ifremer Geo-ocean, 2022. Bathymétrie - Mayotte (synthèse, 2021). https://doi.org/10.12770/0085F83D-CC3E-4C3C-B19A-6C93BCA97BE9
Jung, S.G., Choi, S.H., Ji, K.H., Ryu, J.-S., Lee, D.-C., 2019. Geochemistry of volcanic rocks from Oldoinyo Lengai, Tanzania: Implications for mantle source lithology. Lithos 350–351, 105223. https://doi.org/10.1016/j.lithos.2019.105223
King, R., Floyd, M., Reilinger, R., Bendick, R., 2019. GPS velocity field (MIT 2019.0) for the East African Rift System generated by King et al. https://doi.org/10.1594/IEDA/324785
Lacombe, T., Gurioli, L., Muro, A.D., Médard, E., Berthod, C., Bachèlery, P., Bernard, J., Sadeski, L., Besson, P., Komorowski, J.-C., 2023. The explosive phonolitic volcanism of Petite-Terre (Mayotte, Western Indian Ocean) (preprint). In Review. https://doi.org/10.21203/rs.3.rs-3063558/v1
Lacroix, A., 1922. La constitution lithologique de l'Archipel des Comores, in: CR XIII Ieme Congres International Geologique, Fasc. pp. 949–979.
Le Bas, M.J., 1989. Nephelinitic and Basanitic Rocks. J. Petrol. 30, 1299–1312. https://doi.org/10.1093/petrology/30.5.1299
Le Bas, M.J., Le Maitre, R.W., Streckeisen, A., Zanettin, B., IUGS Subcommission on the Systematics of Igneous Rocks, 1986. A Chemical Classification of Volcanic Rocks Based on the Total Alkali-Silica Diagram. J. Petrol. 27, 745–750. https://doi.org/10.1093/petrology/27.3.745
Leclerc, F., Feuillet, N., Cabioch, G., Deplus, C., Lebrun, J.F., Bazin, S., Beauducel, F., Boudon, G., LeFriant, A., De Min, L., Melezan, D., 2014. The Holocene drowned reef of Les Saintes plateau as witness of a long-term tectonic subsidence along the Lesser Antilles volcanic arc in Guadeloupe. Mar. Geol. 355, 115–135. https://doi.org/10.1016/j.margeo.2014.05.017
Lemoine, A., Briole, P., Bertil, D., Roullé, A., Foumelis, M., Thinon, I., Raucoules, D., de Michele, M., Valty, P., Hoste Colomer, R., 2020. The 2018–2019 seismo-volcanic crisis east of Mayotte, Comoros islands: seismicity and ground deformation markers of an exceptional submarine eruption. Geophys. J. Int. 223, 22–44. https://doi.org/10.1093/gji/ggaa273
Lyubetskaya, T., Korenaga, J., 2007. Chemical composition of Earth's primitive mantle and its variance: 1. Method and results. J. Geophys. Res. 112, B03211. https://doi.org/10.1029/2005JB004223
Masquelet, C., Leroy, S., Delescluse, M., Chamot-Rooke, N., Thinon, I., Lemoine, A., Franke, D., Watremez, L., Werner, P., Paquet, F., Berthod, C., Cabiativa Pico, V., Sauter, D., 2022. The East-Mayotte new volcano in the Comoros Archipelago: structure and timing of magmatic phases inferred from seismic reflection data. Comptes Rendus Géoscience 354, 65–79. https://doi.org/10.5802/crgeos.154
Mazzeo, F.C., Rocco, I., Tucker, R.D., Morra, V., D'Antonio, M., Melluso, L., 2021. Olivine melilitites, mantle xenoliths, and xenocrysts of the Takarindiona district: Petrogenesis, magmatic evolution, and the sub-continental lithospheric mantle of east-central Madagascar. J. Afr. Earth Sci. 174, 104059. https://doi.org/10.1016/j.jafrearsci.2020.104059
Melluso, L., le Roex, A.P., Morra, V., 2011. Petrogenesis and Nd-, Pb-, Sr-isotope geochemistry of the Cenozoic olivine melilitites and olivine nephelinites ("ankaratrites") in Madagascar. Lithos 127, 505–521. https://doi.org/10.1016/j.lithos.2011.08.003
Mertz, D.F., Löhnertz, W., Nomade, S., Pereira, A., Prelević, D., Renne, P.R., 2015. Temporal–spatial evolution of low-SiO2 volcanism in the Pleistocene West Eifel volcanic

field (West Germany) and relationship to upwelling asthenosphere. J. Geodyn. 88, 59–79. https://doi.org/10.1016/j.jog.2015.04.002
Michon, L., 2016. The Volcanism of the Comoros Archipelago Integrated at a Regional Scale, in: Bachelery, P., Lenat, J.-F., Di Muro, A., Michon, L. (Eds.), Active Volcanoes of the Southwest Indian Ocean, Active Volcanoes of the World. Springer Berlin Heidelberg, Berlin, Heidelberg, pp. 333–344. https://doi.org/10.1007/978-3-642-31395-0_21
Michon, L., Famin, V., Quidelleur, X., 2022. Evolution of the East African Rift System from trap-scale to plate-scale rifting. Earth-Sci. Rev. 231, 104089. https://doi.org/10.1016/j.earscirev.2022.104089
Montaggioni, L.F., Nougier, J., 1981. Les enclaves de roches detritiques dans les Volcans d'Anjouan (Archipel des Comores); Origine et interpretation dans le cadre de l'evolution du Canal de Mozambique. Bull. Société Géologique Fr. S7-XXIII, 595–601. https://doi.org/10.2113/gssgfbull.S7-XXIII.6.595
Nehlig, P., Lacquement, F., Bernard, J., Audru, J.-C., Caroff, M., Deparis, J., Jaouën, T., Pelleter, A., Perrin, J., Prognon, C., Benoit, V., 2013. Notice explicative de la carte géologique Mayotte à 1/30 000.
Nougier, J., Cantagrel, J.M., Karche, J.P., 1986. The Comores archipelago in the western Indian Ocean: volcanology, geochronology and geodynamic setting. J. Afr. Earth Sci. 1983 5, 135–145. https://doi.org/10.1016/0899-5362(86)90003-5
Pallares, C., Quidelleur, X., Debreil, J.A., Antoine, C., Sarda, P., Tchilinguirian, P., Delpech, G., Gillot, P.-Y., 2019. Quaternary evolution of the El Tromen volcanic system, Argentina, based on new K-Ar and geochemical data: Insights for temporal evolution of magmatic processes between arc and back-arc settings. J. South Am. Earth Sci. 90, 338–354. https://doi.org/10.1016/j.jsames.2018.12.022
Pavlovsky, R., De Saint Ours, J., 1953. Étude géologique de l'archipel des Comores.
Pelleter, A.-A., Caroff, M., Cordier, C., Bachelery, P., Nehlig, P., Debeuf, D., Arnaud, N., 2014. Melilite-bearing lavas in Mayotte (France): An insight into the mantle source below the Comores. Lithos 208–209, 281–297. https://doi.org/10.1016/j.lithos.2014.09.012
Phethean, J.J.J., Kalnins, L.M., Van Hunen, J., Biffi, P.G., Davies, R.J., McCaffrey, K.J.W., 2016. Madagascar's escape from Africa: A high-resolution plate reconstruction for the Western Somali Basin and implications for supercontinent dispersal: MADAGASCAR'S ESCAPE FROM AFRICA. Geochem. Geophys. Geosystems 17, 5036–5055. https://doi.org/10.1002/2016GC006624
Quidelleur, X., Gillot, P.-Y., Carlut, J., Courtillot, V., 1999. Link between excursions and paleointensity inferred from abnormal field directions recorded at La Palma around 600 ka. Earth Planet. Sci. Lett. 168, 233–242. https://doi.org/10.1016/S0012-821X(99)00061-8
Quidelleur, X., Michon, L., Famin, V., Geffray, M.-C., Danišík, M., Gardiner, N., Rusquet, A., Zakaria, M.G., 2022. Holocene volcanic activity in Anjouan Island (Comoros archipelago) revealed by new Cassignol-Gillot groundmass K–Ar and 14C ages. Quat. Geochronol. 67, 101236. https://doi.org/10.1016/j.quageo.2021.101236
Raczek, I., Stoll, B., Hofmann, A.W., Peter Jochum, K., 2001. High-Precision Trace Element Data for the USGS Reference Materials BCR-1, BCR-2, BHVO-1, BHVO-2, AGV-1, AGV-2, DTS-1, DTS-2, GSP-1 and GSP-2 by ID-TIMS and MIC-SSMS. Geostand. Geoanalytical Res. 25, 77–86. https://doi.org/10.1111/j.1751-908X.2001.tb00789.x
Rasoazanamparany, C., Widom, E., Kuentz, D., Raharimahefa, T., Rakotondravelo, K., Rakotondrazafy, A.M.F., 2021. Geochemistry and mantle source characteristics of the Itasy volcanic field: Implications for the petrogenesis of basaltic magmas in intra-continental-rifts. Geochim. Cosmochim. Acta 300, 137–163. https://doi.org/10.1016/j.gca.2021.02.025
Rasoazanamparany, C., Widom, E., Kuentz, D., Raharimahefa, T., Rakotondrazafy, A.M.F., Rakotondravelo, K.M., 2022. Origin and sources of recent continental alkaline volcanism in

946 the Southwest Ankaratra volcanic field, Central Madagascar: Insights from major and trace
947 element and Sr, Nd, Pb, Hf, Os isotopes. Chem. Geol. 606, 120949.
948 https://doi.org/10.1016/j.chemgeo.2022.120949
949 Rinnert, E., Feuillet, N., Fouquet, Y., Jorry, S., Thinon, I., Lebas, E., 2019. MAYOBS.
950 https://doi.org/10.18142/291
951 Rolandone, F., Poort, J., Masquelet, C., Leroy, S., Thinon, I., Lemoine, A., Paquet, F., 2022.
952 Heat flow measurements in the Northern Mozambique Channel. Comptes Rendus Géoscience
953 354, 35–46. https://doi.org/10.5802/crgeos.130
954 Samper, A., Quidelleur, X., Komorowski, J.-C., Lahitte, P., Boudon, G., 2009. Effusive
955 history of the Grande Découverte Volcanic Complex, southern Basse-Terre (Guadeloupe,
956 French West Indies) from new K–Ar Cassignol–Gillot ages. J. Volcanol. Geotherm. Res. 187,
957 117–130. https://doi.org/10.1016/j.jvolgeores.2009.08.016
958 Samper, A., Quidelleur, X., Lahitte, P., Mollex, D., 2007. Timing of effusive volcanism and
959 collapse events within an oceanic arc island: Basse-Terre, Guadeloupe archipelago (Lesser
960 Antilles Arc). Earth Planet. Sci. Lett. 258, 175–191.
961 https://doi.org/10.1016/j.epsl.2007.03.030
962 Schwarz, W.H., Trieloff, M., 2007. Intercalibration of 40Ar–39Ar age standards NL-25,
963 HB3gr hornblende, GA1550, SB-3, HD-B1 biotite and BMus/2 muscovite. Chem. Geol. 242,
964 218–231. https://doi.org/10.1016/j.chemgeo.2007.03.016
965 Späth, A., Roex, A.P.L., Duncan, R.A., 1996. The Geochemistry of Lavas from the Gomores
966 Archipelago, Western Indian Ocean: Petrogenesis and Mantle Source Region Characteristics.
967 J. Petrol. 37, 961–991. https://doi.org/10.1093/petrology/37.4.961
968 Stamps, D.S., Saria, E., Kreemer, C., 2018. A Geodetic Strain Rate Model for the East
969 African Rift System. Sci. Rep. 8, 732. https://doi.org/10.1038/s41598-017-19097-w
970 Steiger, R.H., Jäger, E., 1977. Subcommission on geochronology: Convention on the use of
971 decay constants in geo- and cosmochronology. Earth Planet. Sci. Lett. 36, 359–362.
972 https://doi.org/10.1016/0012-821X(77)90060-7
973 Strong, D.F., 1972a. Petrology of the Island of Moheli, Western Indian Ocean. Geol. Soc.
974 Am. Bull. 83, 389. https://doi.org/10.1130/0016-7606(1972)83[389:POTIOM]2.0.CO;2
975 Strong, D.F., 1972b. The Petrology of the Lavas of Grande Comore. J. Petrol. 13, 181–218.
976 https://doi.org/10.1093/petrology/13.2.181
977 Thinon, I., Lemoine, A., Leroy, S., Paquet, F., Berthod, C., Zaragosi, S., Famin, V., Feuillet,
978 N., Boymond, P., Masquelet, C., Mercury, N., Rusquet, A., Scalabrin, C., Van der Woerd, J.,
979 Bernard, J., Bignon, J., Clouard, V., Doubre, C., Jacques, E., Jorry, S.J., Rolandone, F.,
980 Chamot-Rooke, N., Delescluse, M., Franke, D., Watremez, L., Bachèlery, P., Michon, L.,
981 Sauter, D., Bujan, S., Canva, A., Dassie, E., Roche, V., Ali, S., Sitti Allaouia, A.H., Deplus,
982 C., Rad, S., Sadeski, L., 2022. Volcanism and tectonics unveiled in the Comoros Archipelago
983 between Africa and Madagascar. Comptes Rendus Géoscience 354, 1–28.
984 https://doi.org/10.5802/crgeos.159
985 Thinon, I., Leroy, S., Lemoine, A., 2021. SISMAORE cruise, Pourquoi pas ? R/V.
986 https://doi.org/10.17600/18001331
987 Thomas, A.L., Fujita, K., Iryu, Y., Bard, E., Cabioch, G., Camoin, G., Cole, J.E., Deschamps,
988 P., Durand, N., Hamelin, B., Heindel, K., Henderson, G.M., Mason, A.J., Matsuda, H.,
989 Ménabréaz, L., Omori, A., Quinn, T., Sakai, S., Sato, T., Sugihara, K., Takahashi, Y.,
990 Thouveny, N., Tudhope, A.W., Webster, J., Westphal, H., Yokoyama, Y., 2012. Assessing
991 subsidence rates and paleo water-depths for Tahiti reefs using U–Th chronology of altered
992 corals. Mar. Geol. 295–298, 86–94. https://doi.org/10.1016/j.margeo.2011.12.006
993 Thompson, R.N., Flower, M.F.J., 1971. One-atmosphere melting and crystallization relations
994 of lavas from Anjouan, Comores Archipelago, Western Indian Ocean. Earth Planet. Sci. Lett.
995 12, 97–107. https://doi.org/10.1016/0012-821X(71)90060-4

Tzevahirtzian, A., Zaragosi, S., Bachèlery, P., Biscara, L., Marchès, E., 2021. Submarine morphology of the Comoros volcanic archipelago. Mar. Geol. 432, 106383. https://doi.org/10.1016/j.margeo.2020.106383

Willbold, M., Stracke, A., 2006. Trace element composition of mantle end-members: Implications for recycling of oceanic and upper and lower continental crust. Geochem. Geophys. Geosystems 7, 2005GC001005. https://doi.org/10.1029/2005GC001005

Woolley, A.R., Bergman, S.C., Edgar, A.D., Le Bas, M.J., Mitchell, R.H., Rock, N.M.S., Scott Smith, B.H., 1996. Classification of lamprophyres, lamproites, kimberlites, and the kalsilitic, melilitic, and leucitic rocks. Can. Mineral. 34, 175–186.

Zinke, J., Reijmer, J.J.G., Thomassin, B.A., 2003. Systems tracts sedimentology in the lagoon of Mayotte associated with the Holocene transgression. Sediment. Geol. 160, 57–79. https://doi.org/10.1016/S0037-0738(02)00336-6